Forced Stationary Planetary Waves in Mars's Winter Atmosphere

JEFFERY L. HOLLINGSWORTH

NASA/Ames Research Center, Moffett Field, California

JEFFREY R. BARNES

College of Oceanic and Atmospheric Sciences, Oregon State University, Corvallis, Oregon

(Manuscript received 8 October 1993, in final form 10 August 1995)

ABSTRACT

Mariner 9 and *Viking* spacecraft observations provided evidence for planetary-scale, wavelike disturbances in the Mars winter atmosphere. Possible sources of the wave activity are dynamical instabilities, for example, barotropic and/or baroclinic instabilities. Other candidate sources are forced, quasi-stationary planetary waves—waves that arise predominantly via zonally asymmetric surface properties. The authors attempt to model aspects of the wave activity, focusing on forced planetary waves in representative wintertime atmospheres for Mars, by applying a spherical linear primitive equations model. Basic states representing relatively "nondusty" and "highly dusty" conditions near winter solstice allow wavenumber 1 and 2 disturbances to propagate meridionally and vertically about the jet. Higher wavenumbers are strongly vertically trapped. Stationary waves during winter in the northern and southern extratropics differ strongly in amplitude, phase, and dominant horizontal wave pattern. Northern extratropical eddies exhibit a definite wavenumber 2 pattern with comparable amplitudes for wavenumbers 1 and 2. Southern eddies, however, are very strongly dominated by wavenumber 1. Because of enhanced refractive properties of the dusty basic state, dusty responses are an order of magnitude larger than nondusty ones. Horizontal and meridional wave propagation is illuminated by diagnostics for the wave activity flux, for example, Eliassen–Palm and Plumb fluxes. As a result of the separation distance between major orographic features on Mars, together with a planetary waveguide that enhances zonal propagation, Rossby wave interferences between western and eastern hemispheric wave trains occur. This analysis is relevant to future global mapping missions to Mars (e.g., polar-orbiting spacecraft) that will return key atmospheric observations of planetary wave activity.

1. Introduction

Of all the planets, in many ways Mars is the most similar to Earth. Mars's size is nearly half of Earth's and both planets have very similar rotation rates. A comparison of fundamental planetary and atmospheric parameters for the two planets is listed in Table 1. Mars's highly elliptical orbit has important implications for its climate: as the planet revolves about the Sun, not only does it spend more time at aphelion than at perihelion, but the amount of sunlight reaching the top of the atmosphere is roughly 40% weaker (Leovy 1985). Combined with the planet's axial tilt, the orbital geometry produces a sizeable seasonal asymmetry in incoming solar radiation between the northern and southern hemispheres. However, the similar sizes and rotation rates makes comparisons between the two atmospheric circulations meaningful.

Corresponding author address: Dr. Jeffery L. Hollingsworth, NASA/Ames Research Center, MS: 245-3, Moffett Field, CA 94035-1000.
E-mail: jeffh@humbabe.arc.nasa.gov

In contrast with Earth's atmosphere, there has been limited study of stationary planetary waves in the atmosphere of Mars. In part, this can be attributed to a paucity of detailed observations. The *Mars Observer* spacecraft would have returned detailed observations in which planetary-scale disturbances, both stationary and traveling, could have been discernible. In addition, a better knowledge of the sources of forced wave activity would have been obtained, such as high-resolution topography in particular (Albee and Palluconi 1990). Prior to the next global mapping missions to Mars, it is important to study forced planetary waves in Mars's atmosphere with realistic dynamical models that can both reveal an essential aspect of its atmospheric circulation and provide a benchmark for new data. Since Mars and Earth have similar fundamental parameters (e.g., rotation rate, size, atmospheric scale height), such investigations can also provide a comparative "test" of our understanding of forced planetary waves.

Conrath (1981) detected large-scale wave phenomena in Mars's atmosphere by examining *Mariner 9* Infrared Interferometer Spectrometer (IRIS) temperature data for late northern winter. Because of the observing

sequence and data limitations, it was not possible to uniquely determine the zonal wavenumber and frequency associated with any disturbance. The data did, however, permit a search for disturbances exhibiting a deep, hemispheric structure. An example of a significant deviation isolated from the mean thermal state is reproduced in Fig. 1. As discussed by Conrath, an infinite number of combinations of wavenumber and frequency could correspond to this particular disturbance. Possible modes were a very slow, westward propagating wavenumber 1 and a stationary wavenumber 2. Whether the phenomenon was due to an in situ shear instability (e.g., barotropic and/or baroclinic) or possibly to a forced quasi-stationary wave (e.g., topographically and/or thermally forced) remains uncertain.

Past spacecraft observations have established that Mars has large and highly variable relief on "continental" scales (Hanel et al. 1972; Conrath et al. 1973; Wu 1978), with topographic heights exceeding an atmospheric-scale height in the Tharsis region of the western hemisphere's tropics. Previous studies have utilized the available topography data within dynamical models to explore the character of forced planetary waves for Mars. Using an analytic model, Blumsack (1971) considered the effects of variable topography on Mars's steady large-scale, midlatitude circulation and determined that high (low) elevations could be associated with thermal troughs (ridges). Focusing on Mars's southern hemisphere, Mass and Sagan (1976) incorporated preliminary *Mariner 9* topography into a two-level, quasigeostrophic model and found high-pressure regions positioned on the upslopes of high relief (e.g., Tharsis and Noachis Terra). The features exhibited an intensification and weak westward tilt with height. Applying a linear quasigeostrophic model with a simple cosine(latitude) mean basic state, Gadian (1978) determined wave responses forced by a coarse Fourier mode–decomposed topography. Wavenumber 2 obtained sizeable amplitudes and showed weak westward phase variation. In a different study, Webster (1977) applied a steady-state, linear, two-level primitive equations model and considered both mechanical and thermal effects of topography. The northern winter circulation exhibited large amplitude stationary features in low and middle latitudes. As evidenced at the two model levels, the stationary eddies were strongly barotropic. Also, the forced responses during southern winter indicated similar magnitudes and spatial patterns.

TABLE 1. Basic planetary and atmospheric parameters for Mars and Earth.

Basic Parameter	Mars	Earth
Planetary radius (km)	3394	6369
Gravit. accel. (m s^{-2})	3.72	9.81
Orbital inclin. (°)	25.2	23.5
Length of year (days)	687	365
Rotation rate ($\times 10^{-5}$ s^{-1})	7.088	7.292
Solar constant (W m^{-2})	591	1373
Main constituents	CO_2 (0.95), N_2 (~0.02)	N_2 (0.78), O_2 (0.21)
Equilib. temp (K)	210	256
Gas const. (J K^{-1} kg^{-1})	191	287
Scale height (km)	10.0	7.8
Avg lapse rate (K km^{-1})	2.5	6.5
Surface pressure (mb)	6–8	1013
Temp near surface (K)	145–245	220–310

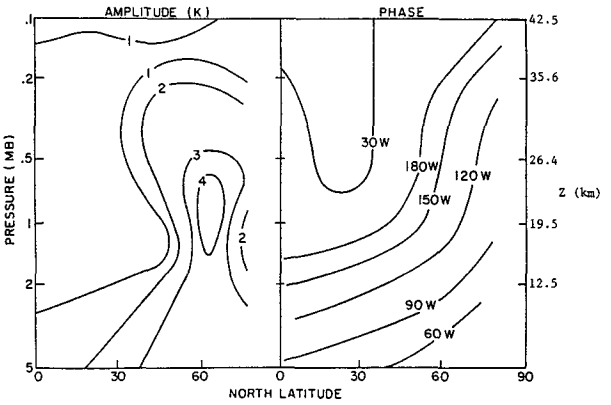

FIG. 1. Meridional structure of a temperature wave as observed by the *Mariner 9* IRIS (a) wave amplitude $|T'|$ (K) and (b) phase (°W) assuming a stationary, zonal wavenumber 2 disturbance (from Conrath 1981).

General circulation models having various spatial resolutions and including complex physical processes (e.g., radiative heating by atmospheric dust) have also been adapted to Mars. Both thermally (e.g., Leovy and Mintz 1969; Moriyama and Iwashima 1980) and mechanically (Pollack et al. 1981; Pollack et al. 1990) forced, large amplitude nearly stationary waves have been predicted to occur in the winter sub- and extratropics. The simulated stationary waves in midlatitudes frequently exhibit a mostly barotropic structure and pronounced southwest (east)–northeast (west) tilt at low levels (e.g., below 10 km) for northern (southern) winter.

In this paper, we investigate forced, stationary planetary waves in Mars's winter atmosphere by applying a spherical, linear primitive equations (LPE) model. Although a steady, linear approach undoubtedly simplifies the nature of the forced wave dynamics, a linear model does allow a consistent separation of the wave response into different elements that make up the total forcing mechanism. The model has much higher vertical resolution than previous linear studies for Mars, incorporates the best available topography datasets, and uses mean zonal basic states with considerable meridional structure that represent our best estimate of winterlike conditions. A better grasp of atmospheric winds on Mars must await future mapping missions of the

planet's atmosphere. Prior to such missions, it is useful to consider wave propagation into plausible mean flows based on the observations available.

The plan of the paper is as follows. In the next section, the dynamical model is described. In section 3, representative winter basic states for Mars are constructed, and features of the available global topography datasets are summarized. Stationary wave calculations for relatively nondusty Mars wintertime conditions are presented in section 4. In the subsequent section, an assessment is made of potential global responses and wave interferences. Section 6 presents results for highly dusty conditions. The last section contains a summary and conclusions.

2. Model

The dynamical model is based on the primitive equations expressed in log-pressure coordinates (e.g., Andrews et al. 1987). For linearized disturbances, the equations are

$$\bar{D}u' + v'\left[\frac{(\bar{u}\cos\varphi)_\varphi}{a\cos\varphi} - f\right] + w'\bar{u}_z + \frac{1}{a\cos\varphi}\Phi'_\lambda - X' = 0 \quad (1)$$

$$\bar{D}v' + u'\left(\frac{2\bar{u}\tan\varphi}{a} + f\right) + \frac{1}{a}\Phi'_\varphi - Y' = 0 \quad (2)$$

$$\Phi'_z - \frac{R}{H}\theta' e^{-\kappa z/H} = 0 \quad (3)$$

$$\frac{u'_\lambda + (v'\cos\varphi)_\varphi}{a\cos\varphi} + \frac{1}{\rho_0}(\rho_0 w')_z = 0 \quad (4)$$

$$\bar{D}\Phi'_z + \frac{v'}{a}\bar{\Phi}_{z\varphi} + N^2 w' - \frac{\kappa}{H}J' = 0. \quad (5)$$

The overbar and prime denote zonal means and departures from the zonal mean, respectively. Here, $z = -H \times \ln(p/p_s)$, the vertical coordinate in log-pressure coordinates; H is a constant scale height; p_s is a constant reference pressure; Φ is the geopotential; θ is the potential temperature; a is the planetary radius; κ is the ratio of the gas constant R to the specific heat at constant pressure c_p; $f = 2\Omega\sin\varphi$, the Coriolis parameter; and Ω is the planetary rotation rate. Variables (u, v, w) are the eastward (zonal), northward (meridional), and vertical ($w = dz/dt$) velocity components corresponding to (λ, φ, z), the longitudinal, latitudinal, and vertical coordinates, respectively. In addition, $\rho_0 = \rho_s e^{-z/H}$, where ρ_s is a constant density; $\bar{D}(\ ) \equiv (\ )_t + (a\cos\varphi)^{-1}\bar{u}(\ )_\lambda$; and the log-pressure buoyancy frequency is defined as $N^2 = N^2(\varphi, z) \equiv RH^{-1}\bar{\theta}_z e^{-\kappa z/H}$. Equations (1)–(5) describe the horizontal momentum balance, hydrostatic balance, mass continuity, and the thermodynamic energy equation, respectively. Horizontal nonconservative mechanical forcing is specified as (X', Y'). The diabatic heating rate per unit mass is J'. Choices for these terms are described below.

For a basic flow, a steady, zonally symmetric flow is prescribed that is purely zonal and unforced [a gradient wind–balanced $\bar{u}(\varphi, z)$]. Choices for mean basic states for Mars are described in the next section.

In order to solve (1)–(5), dependent variables are decomposed in terms of Fourier modes in longitude, and time and *steady* solutions are sought of the form, for example, for Φ',

$$\Phi'(\lambda, \varphi, z, t) = \sum_{s=1}^{\infty} \mathrm{Re}[\hat{\Phi}(\varphi, z)\, e^{i(s\lambda - 2\Omega\sigma t) + z/2H}], \quad (6)$$

where $\hat{\Phi}$ is in general complex. For a *stationary* calculation, $\sigma = 0$. Using this representation and following Lin (1982), the equations are combined, and for each Fourier mode, a single structure equation in terms of the geopotential amplitude is formed

$$A\hat{\Phi}_{\varphi\varphi} + B\hat{\Phi}_{\varphi z} + C\hat{\Phi}_{zz} + D\hat{\Phi}_\varphi + E\hat{\Phi}_z + F\hat{\Phi} = G, \quad (7)$$

where the coefficients $A, B, \ldots, F$ are functions of (φ, z) through their dependence on the basic flow: G depends on the specified forcings J', X', and Y'. Explicit expressions for the coefficients $A, B, \ldots, F$ in terms of nondimensional basic flow quantities can be found in Lin (1982) and Hollingsworth (1992).

Using (7), the linear and steady-state wave structure is determined in a global domain subject to a particular set of boundary conditions. At the poles, it is assumed that $\Phi' = 0$. At the upper boundary, $z_T = 100$ km, it is also assumed that $\Phi' = 0$. At the lower boundary, $z_B = 2$ km, the thermodynamic energy equation (5) is applied together with a kinematic condition.

In terms of the *geometric* vertical velocity $\tilde{w}$, the kinematic condition used is

$$\tilde{w} = \boldsymbol{v}_B \cdot \nabla h_B = \frac{u_B}{a\cos\varphi} h_{B\lambda} + \frac{v_B}{a} h_{B\varphi}, \quad (8)$$

where h_B is the planetary orography and $\boldsymbol{v}_B$ is the flow at the surface. This condition is not really applied at the surface but at a fixed log-pressure height $z = z_B$ (an approximation that could be removed by using terrain-following coordinates, e.g., $\sigma = p/p_s$). Because the model is formulated with a log-pressure vertical coordinate, it is necessary to relate the geometric vertical velocity in (8) to the log-pressure vertical velocity (w)

$$\tilde{w} = \frac{1}{g}\left(\Phi_t + \frac{u}{a\cos\varphi}\Phi_\lambda + \frac{v}{a}\Phi_\varphi + w\Phi_z\right). \quad (9)$$

Linearizing (8) and (9) about the basic zonal flow gives

$$\tilde{w}' = \frac{\bar{u}_B}{a\cos\varphi} h'_{B\lambda} + \frac{v'_B}{a}\bar{h}_{B\varphi} \quad (10)$$

and

$$\tilde{w}' = \frac{1}{g}\left(\bar{D}\Phi' + \frac{v'}{a}\bar{\Phi}_\varphi + w'\bar{\Phi}_z\right). \quad (11)$$

Combining the above two equations for $\tilde{w}'$ at $z = z_B$, the model's lower boundary, and eliminating w' between this result and (5), the modified thermodynamic energy equation is obtained:

$$\bar{D}_B(\Phi'_{Bz} - \bar{h}^{-1}\Phi'_B) + \frac{v'_B}{a}(\bar{\Phi}_{Bz\varphi} - \bar{h}^{-1}\bar{\Phi}_{B\varphi}) = \frac{\kappa}{H}J'_B - \frac{g}{\bar{h}}\left(\frac{\bar{u}_B h'_{B\lambda}}{a\cos\varphi} + \frac{v'_B\bar{h}_{B\varphi}}{a}\right), \quad (12)$$

which forms the lower boundary condition. Here, $\bar{h}^{-1} \equiv N^2/\bar{\Phi}_{Bz}$.

As detailed in section 3, Mars has substantial large-amplitude topography in the tropics. Whether a linear approach is vastly inadequate to determine the *extratropical* stationary wave response is a valid concern. We return to this issue in our discussion of results in section 4. We note here that the linearized form of $\tilde{w}'$ as expressed by (10) has a term proportional to the zonal-mean topography $\bar{h}_{B\varphi}$, which is often neglected in terrestrial linear planetary wave models. For Mars this can make a significant contribution, particularly in the northern hemisphere.

Simple choices are made for the external physics used in the model. Radiative heating is parameterized in terms of a Newtonian cooling with height-dependent rate relaxation coefficients $\alpha_N(z)$ as determined by Barnes (1984) for relatively nondusty and highly dusty conditions. Specifically, in the thermodynamic energy equation, we set $\kappa H^{-1}J' = -\alpha_N\Phi'_z$. In addition, dissipation of wave momentum is provided through damping via Rayleigh friction. Nonconservative mechanical forcings in (1) and (2) are prescribed with $(X', Y') = -\alpha_R(z)(u', v')$, and the vertically dependent "drag" coefficients are largest at high levels. The use of a momentum drag also provides for an effective "sponge layer" in the upper part of the model, absorbing upward propagating wave energy and inhibiting wave reflection from the model top. Values of the height-dependent Rayleigh friction coefficients used are assumed to be typically less than those of the Newtonian cooling coefficients. Choices for the dissipation profiles are shown in Fig. 2.

With the aforementioned boundary conditions, (7) can be discretized using centered finite differences on a hemispheric latitude–height grid. The finite-difference form of the wave structure equation results in a system of algebraic equations that can be expressed in block tridiagonal form and solved using an algorithm of Lindzen and Kuo (1969). In the calculations, a nominal grid spacing of $\Delta\varphi = 4°$ latitude and $\Delta z = 2$ km is used. Sensitivity experiments using finer grid spacings have indicated that the results are only slightly changed (e.g., wave amplitudes are decreased by 15%–20% for a factor of 4 decrease in $\Delta\varphi$).

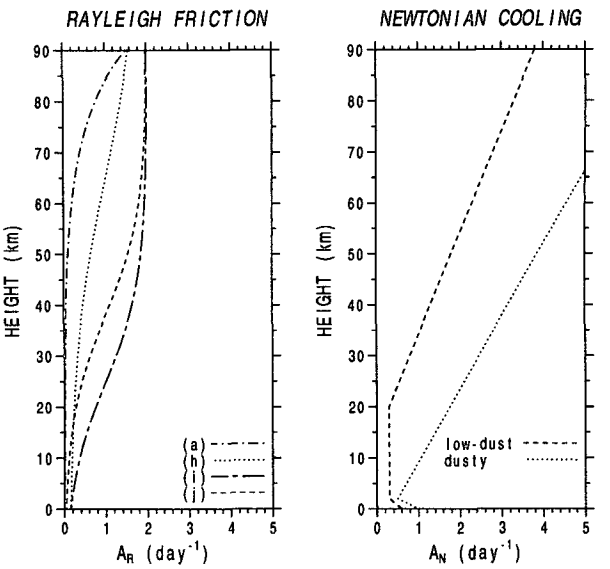

FIG. 2. Profiles of (a) the Rayleigh friction coefficient, α_R (day^{-1}), and (b) the Newtonian cooling coefficient, α_N (day^{-1}), used in the linear model.

3. Winter basic states and planetary wave forcings

a. *Mean flows*

Late winter time series of atmospheric temperature for the northern hemisphere indicate the presence of a mean zonal temperature gradient between low and high latitudes, with temperature decreasing toward the pole (Conrath 1981; Santee and Crisp 1993). By thermal wind balance, such a temperature distribution will support a spatially varying westerly flow that intensifies with height. Reproduced from Conrath (1981) and Michelangeli et al. (1987) in Fig. 3 are the observed $\bar{T}$ and gradient-balanced $\bar{u}$ cross sections, assuming $\bar{u} = 0$ at the 5-mb level. Warmer temperatures are found in low latitudes and low altitudes, and a nearly isothermal atmosphere occurs in high northern latitudes. The region of maximum temperature slopes upward and poleward from the subtropics. Accompanying this thermal pattern is an increasing static stability from low latitudes toward middle and high latitudes, with the maximum stability sloping upward and poleward. Because the mean wind field at one boundary level is unknown, the true magnitude of the westerly jet is indeterminate.

Nevertheless, Mars's winter atmosphere ought to support a westerly waveguide permitting planetary waves forced via large-scale zonal asymmetries near the planet's surface to propagate vertically and meridionally. In a β-plane geometry, Conrath (1981) constructed the quasigeostrophic refractive index for the

winter zonal-mean cross section deduced from *Mariner 9*. In midlatitudes, wavenumber 2 could penetrate up to about 0.5 mb (~25 km). In high northern latitudes (poleward of 60°N), propagation would be unfavored. Although wave propagation in spherical geometry can be very different than in β-plane geometry, Conrath's analysis indicates that stationary waveguides exist for a smoothed version of Mars's late winter westerly vortex.

The basic states that are applied in this study emulate that depicted in Fig. 3 and are shown in Fig. 4. Results from several independent dynamical models developed to investigate Mars's atmospheric circulation—2D models that have examined the zonally symmetric circulation (e.g., Haberle et al. 1982) and versions of an improved Mars general circulation model (MGCM) (e.g., Pollack et al. 1990; Barnes et al. 1993)—provided constraints for the construction of the idealized flows. The flows have a "tilted" structure where the magnitude of the zonal wind increases with increasing latitude and increasing height. The strength of the "surface" zonal winds roughly agrees with near-surface zonal winds determined from solsticial MGCM experiments with little and enhanced dust loading. Generally, the nondusty flow is weaker than the dusty basic flow, and the latter has its jet core shifted slightly poleward from the former. It is known from both 2D modeling (Haberle et al. 1982) and general circulation simulations (Haberle et al. 1993) of Mars that during periods of increased atmospheric dust loading the zonally symmetric circulation intensifies significantly. In particular, the thermal maximum located in midlatitudes and middle-atmospheric levels shifts poleward by 5°–10° and the extratropical horizontal temperature gradient is strengthened. Accompanying those changes in thermal structure is a more vigorous zonal jet that shifts slightly poleward. Similar changes in middle- and high-latitude temperatures have been observed by the *Viking Orbiters* near 0.6 mb during periods of increased atmospheric dust loading (Martin and Kieffer 1979; Jakosky and Martin 1987).

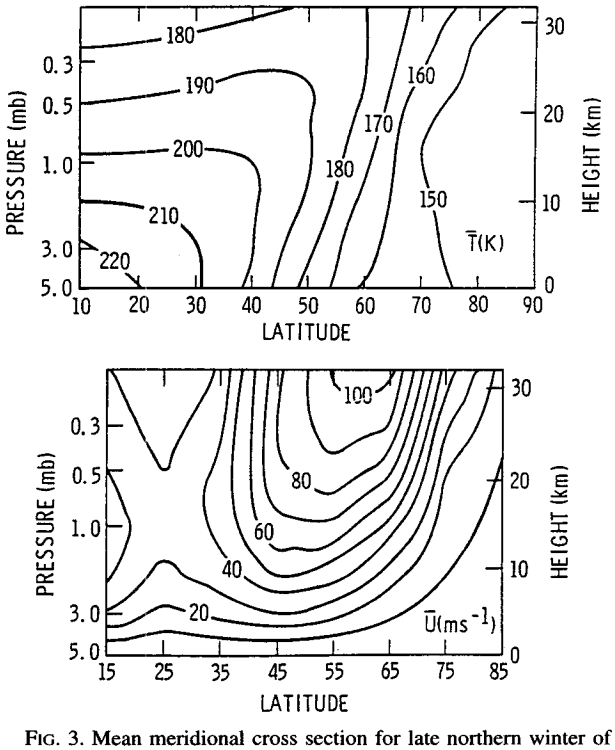

FIG. 3. Mean meridional cross section for late northern winter of (a) temperature $\bar{T}$ (K) as derived from *Mariner 9* IRIS data and (b) calculated gradient balanced zonal-mean zonal wind $\bar{u}$(m s^{-1}) assuming that the 5-mb level $\bar{u} = 0$ (from Michelangeli et al. 1987).

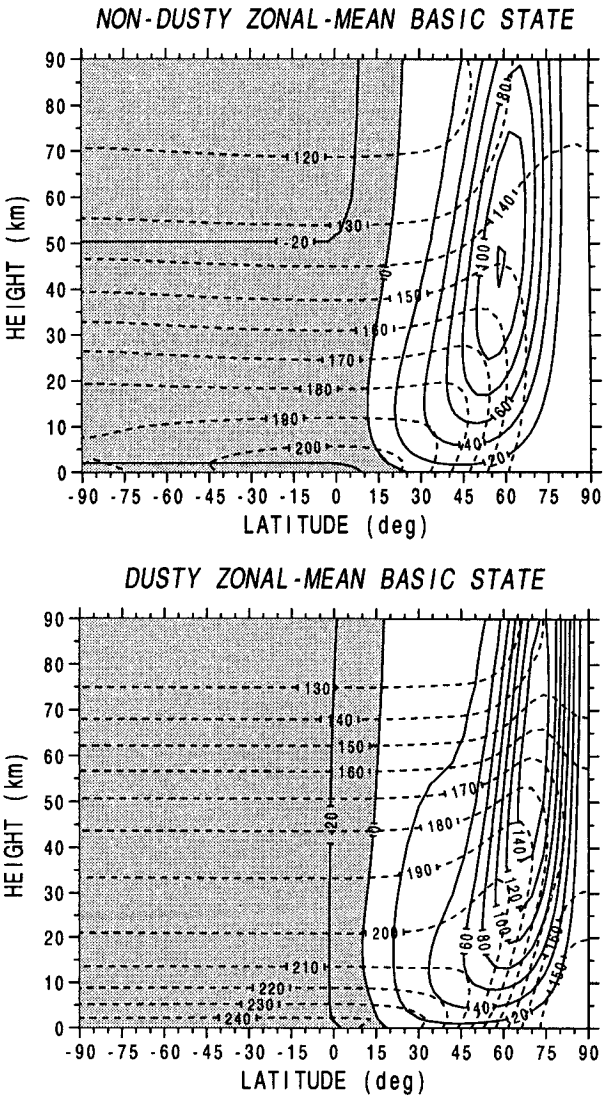

FIG. 4. Relatively nondusty (a) and dusty (b) basic flows used in the linear model (m s^{-1}). Negative values are shaded. Dashed contours correspond to gradient wind–balanced temperatures (K).

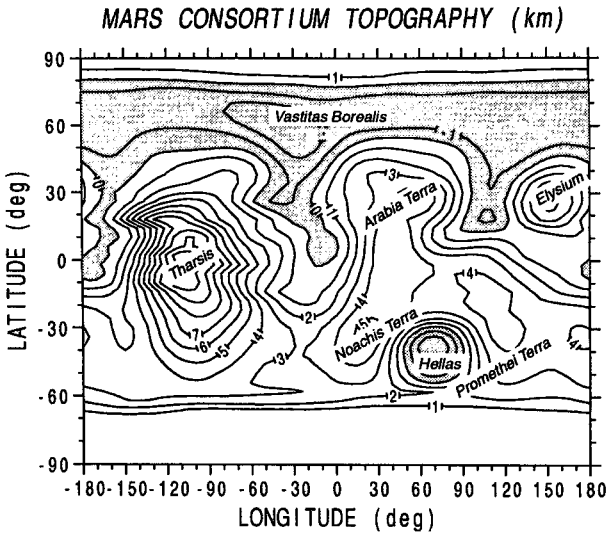

FIG. 5. Smoothed Mars Consortium topography (km) composited from the first six zonal harmonics (s = 0–5). Negative values are shaded.

Fundamental to planetary wave propagation is the latitudinal gradient of planetary vorticity, β. For spherical wave propagation on zonally symmetric basic flows having vertical and meridional structure, the effective beta (i.e., $\bar{q}_\varphi$) can be much different from that associated only with solid-body rotation. Strong meridional curvatures of the mean flow ($-a^{-1}\bar{u}_{\varphi\varphi} > 0$) can contribute to regions of $\bar{q}_\varphi > 0$ centered through a symmetric jet. For the stronger dusty flow shown in Fig. 4, the positive channel of $\bar{q}_\varphi$ is enhanced.

b. *Wave forcings*

In Mars's northern hemisphere, two main large-scale topographic features are the high-relief regions in middle latitudes (protrusions of Tharsis in the western hemisphere and Arabia Terra in the eastern hemisphere) and Vastitas Borealis in high latitudes (a longitude-encircling "trough" on the order of 1 km below the 6.1-mb standard topographic datum). These features are clearly shown in Fig. 5. In the southern hemisphere, Tharsis and the low relief in the Hellas basin constitute the primary features. Because of steep zonal slopes on the western and eastern flanks of the latter, the regions of Noachis and Promethei Terra could be important in the large-scale stationary circulation in southern midlatitudes.

As the primary topography used in this study, we choose the Mars Consortium dataset (Kieffer et al. 1982). The topographic data were determined by several instruments from the *Mariner 9* mission (e.g., infrared and ultraviolet spectroscopy, and radio occultation), Earth-based radar, and stereophotogrammetry. Details on the compilation and quality of the data are provided in Wu (1978). Typical vertical errors range from 500 m in low latitudes to near 2 km in polar regions. The smoothed topography shown in Fig. 5 was produced by a Fourier analysis of this dataset, truncating after six zonal harmonics (i.e., s = 0–5). Prior to Fourier decomposition, the 1° × 1° global data were averaged into 4° latitudinal bins, and the calculations were then carried out to zonal wavenumber 10. Figure 6 shows a plot of the topographic Fourier amplitudes as a function of zonal wavenumber and latitude. The lower "planetary" wavenumbers dominate the zonal variability spectrum, and the amplitudes are largest in the tropics. The strongest component is associated with zonal wavenumber 2. And, wavenumber 1 is 3–4 times stronger in southern midlatitudes compared to that in the north.

4. Relatively nondusty results

Results for the relatively nondusty basic state are presented in this section. To represent extratropical features corresponding to the largest zonal scales, the calculations have been carried out to zonal wavenumber 5.

a. *Northern topographic response*

For northern winter, strong vertical wave propagation occurs for zonal wavenumbers 1 and 2, whereas larger wavenumbers penetrate less readily. This can be seen in the wave geopotential amplitudes shown in Fig. 7. A moderately weak Rayleigh friction [profile (j) in Fig. 2a] and the low-dust Newtonian cooling were used in the calculation. Wavenumber 1 shows a maximum amplitude located in winter high latitudes at 60–70 km,

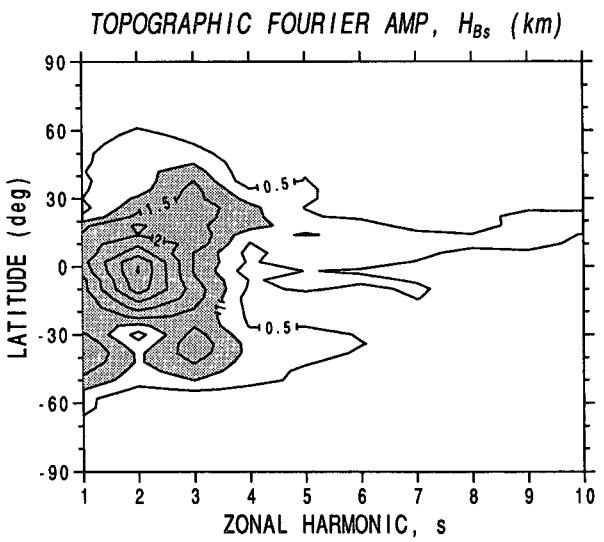

FIG. 6. The topographic Fourier amplitudes as a function of wavenumber s and latitude φ for wavenumbers 1–10. Values greater than 1 km are shaded.

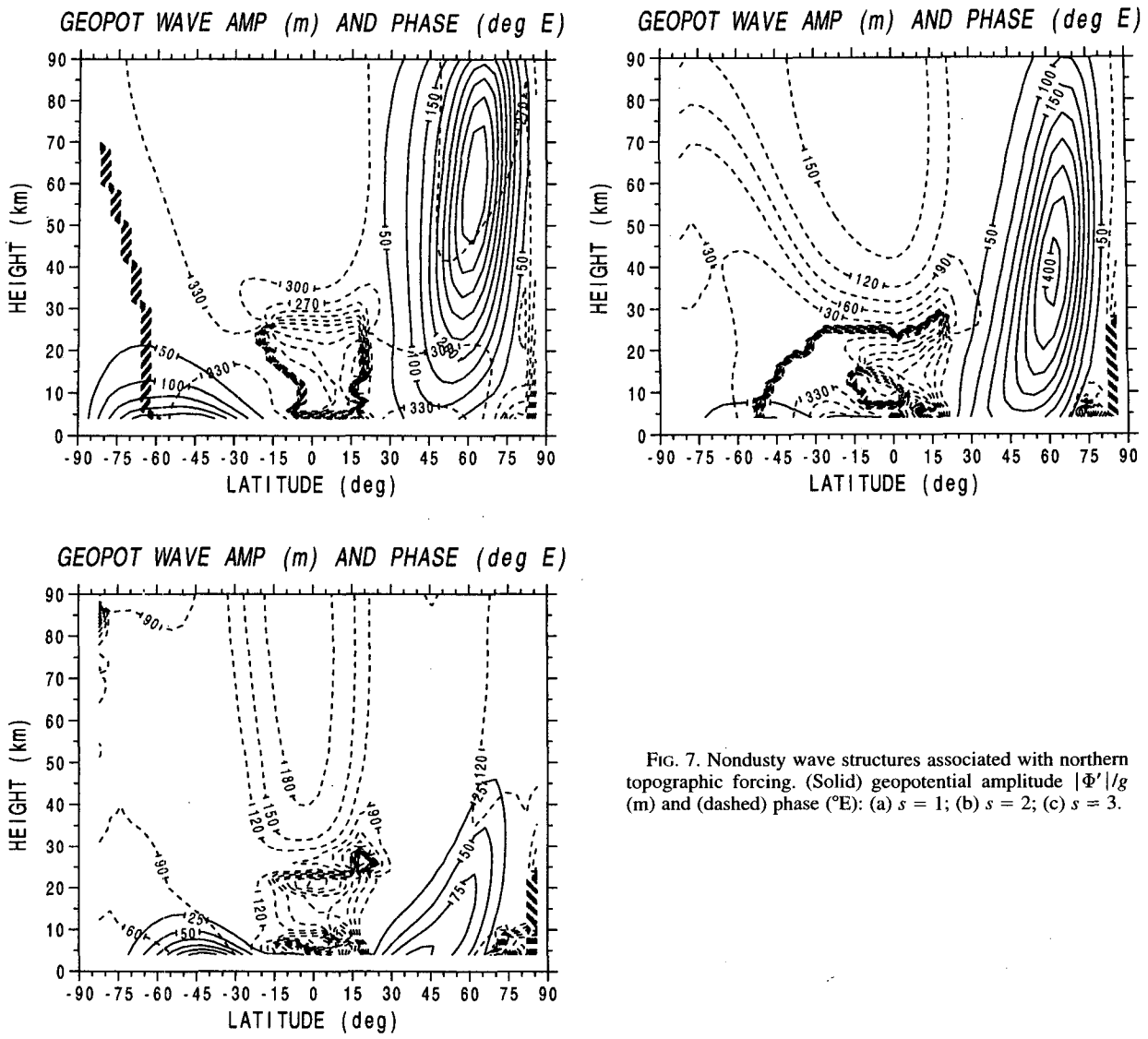

FIG. 7. Nondusty wave structures associated with northern topographic forcing. (Solid) geopotential amplitude $|\Phi'|/g$ (m) and (dashed) phase (°E): (a) $s = 1$; (b) $s = 2$; (c) $s = 3$.

and its phase exhibits a westward tilt with increasing height. Also evident is pronounced vertical trapping within the easterlies of the summer hemisphere. For wavenumber 2, a large amplitude is also found in high latitudes but it peaks roughly 20 km lower than wavenumber 1. It can also be seen that wavenumber 2 is quite barotropic: there is less than a 10° westward shift below 90 km. Wavenumber 3 also appears strongly vertically trapped below 30–40 km in winter midlatitudes.

The stationary wavenumber 1 and 2 temperature amplitudes corresponding to the above geopotential fields range between 1 and 3 K; peak near 30 and 10 km, respectively; and occur at the same latitude as the strongest values of $\bar{u}(\varphi, z)$. For wavenumber 2, the peak amplitude occurs 10–15 km lower than in the *Mariner 9* IRIS observations (cf. Fig. 1), and there is essentially no phase variation in middle and high latitudes.

Sensitivity experiments indicate that the vertical positions of the amplitude maxima are insensitive to the momentum drag strength below the jet core. However, the jet core's vertical position does affect their location. For example, with a jet having similar meridional structure but peaking 10–20 km lower, both the wavenumber 1 and 2 maximum amplitudes occurred correspondingly lower. Wavenumber 3 was unchanged.

The tendency for greater vertical propagation for the lower zonal wavenumbers is generally consistent with the Charney–Drazin condition (Charney and Drazin 1961). A more physically revealing quantity describing potential vertical and meridional wave propagation is the modified quasigeostrophic refractive index, $\tilde{Q}_s$ (Palmer 1981, 1982):

$$\tilde{Q}_s(\varphi, z) = \frac{1}{\sin^2\varphi}\left(\frac{a\bar{q}_\varphi}{\bar{u}} - \frac{s^2}{\cos^2\varphi} - \frac{a^2\tilde{\epsilon}}{4H^2}\right), \quad (13)$$

where $\tilde{\epsilon} = f^2/N^2$. Key to this diagnostic is the ratio of the latitudinal gradient of mean zonal quasigeostrophic potential vorticity $a^{-1}\bar{q}_\varphi$ and the mean zonal wind $\bar{u}$. Wave propagation (evanescence) is favored in regions of large and positive (negative) $\tilde{Q}_s$. The "defocusing" term of the refractive index, $\tilde{Q}_s \sim -s^2 \cos^{-2}\varphi$, represents an efficient barrier to wave propagation for large zonal wavenumbers or in high latitudes. Shown in Fig. 8 are the refractive index patterns associated with the nondusty flow and zonal wavenumbers 1–3. For both wavenumbers 1 and 2, a positive waveguide extends upward from low levels in middle latitudes toward high levels in high latitudes. The wavenumber 1 waveguide is quite similar to a positive channel of $\bar{q}_\varphi$ due primarily to the mean zonal flow's strong (and negative) meridional curvature. For wavenumber 3, the waveguide is completely absent in the vertical, except below 10–15 km in midlatitudes. The form of the refractive index shown in Fig. 8 does not explicitly include a dependence on dissipation (e.g., as in Schoeberl and Geller 1977). However, provided $\alpha_R \ll s\bar{u}/(a\cos\varphi)$ (as is the case here), the inviscid form of $\tilde{Q}_s$ is a good approximation. From the dependence of $\tilde{Q}_s$ on the zonal wavenumber, deep vertical penetration should not be expected for $s > 2$.

The Eliassen–Palm (EP) wave activity flux $\mathbf{F}$ (Edmon et al. 1980; Dunkerton et al. 1981; Palmer 1982) and "wave driving" $D_F = (\rho_0 a\cos\varphi)^{-1}\nabla\cdot\mathbf{F}$ can further reveal aspects of the meridional wave propagation. Expressions for their spherical primitive equations forms can be found in Andrews et al. (1987). Figure

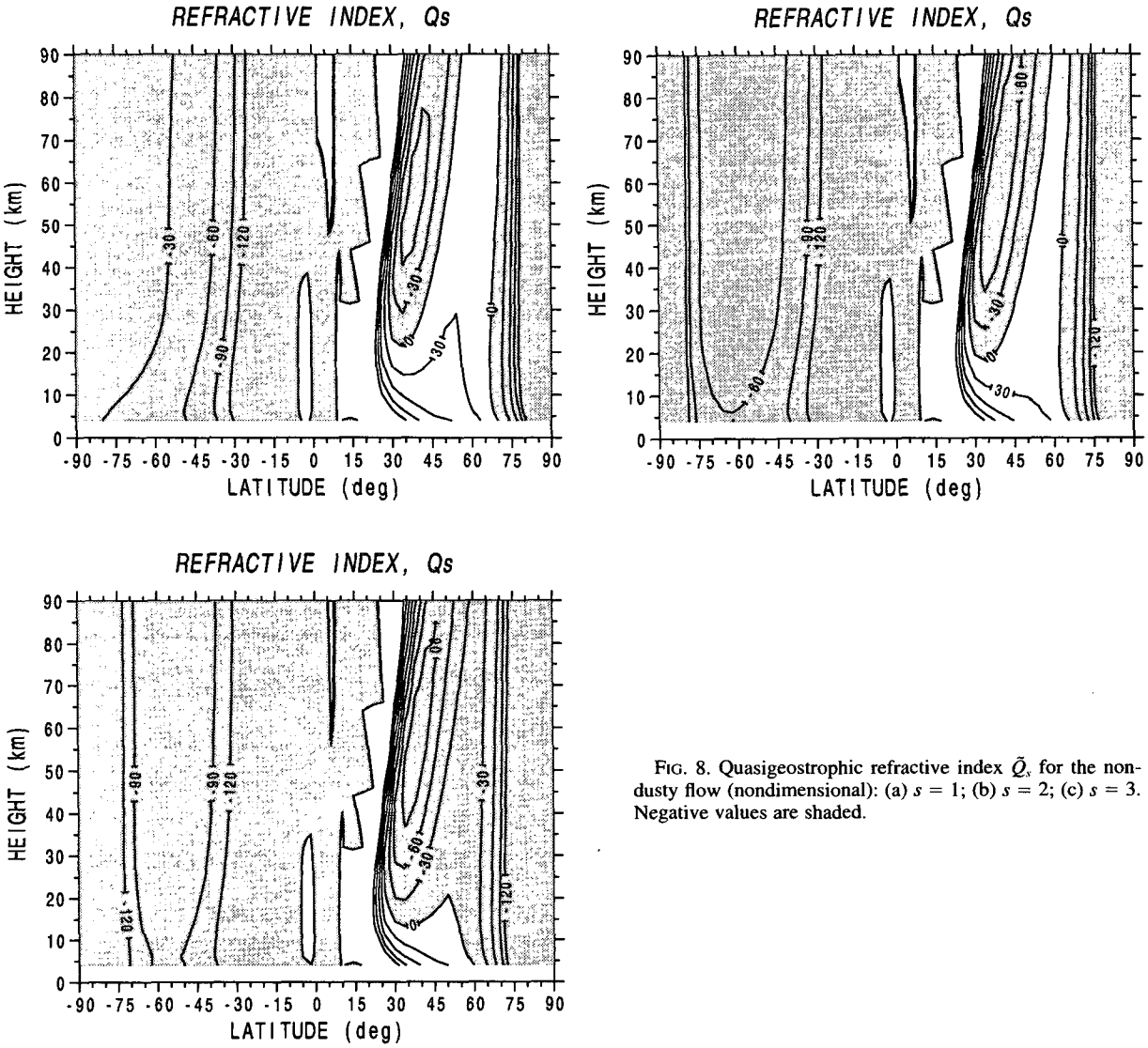

FIG. 8. Quasigeostrophic refractive index $\tilde{Q}_s$ for the nondusty flow (nondimensional): (a) $s = 1$; (b) $s = 2$; (c) $s = 3$. Negative values are shaded.

9 shows a composite cross section using flux contributions from zonal wavenumbers 1–3. A standard convention is used to plot the EP flux in the meridional plane (e.g., Dunkerton et al. 1981; Butchart et al. 1982). In Fig. 9, the flux emanates out of the midlatitudes and, by 20–30 km, is directed equatorward in middle and low latitudes and mostly upward in high latitudes. The upward pattern is due primarily to wavenumber 1 and is consistent with a poleward heat flux evident in this component's westward phase tilt with increasing height (cf. Fig. 7). Partial wave reflection off the waveguide's equatorward barrier where $\tilde{Q}_s < 0$ can also be seen (cf. Fig. 8a). In this region, the phase tilts westward with increasing latitude above 50 km. As indicated in the D_F field, a convergence of wave activity occurs within the extratropical waveguide and exerts a weak deceleration of $\bar{u}$, mostly in high levels. Although not shown, the net linear tendency $\bar{u}_t$ associated with the residual mean meridional circulation (0, $\bar{v}^*$, $\bar{w}^*$) (i.e., that due to wave forcing and an induced meridional circulation) is somewhat weaker. Under nominal nondusty conditions, therefore, topographically forced steady stationary waves would exert only modest wave driving in the winter extratropics.

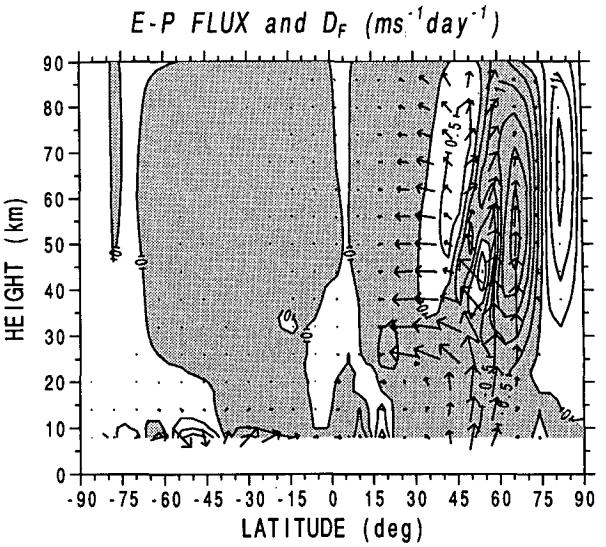

FIG. 9. Nondusty EP flux **F** and wave driving D_F (m s^{-1} day^{-1}) associated with northern topographic forcing: **F** has been normalized by ρ_0 (z), and negative D_F values are shaded.

A zonally oriented wave pattern is the response in northern midlatitudes, with a strong wavenumber 2 signature, as can be seen in Fig. 10. Above 30 km, the pattern becomes predominantly wavenumber 1. The stationary features appear asymmetric between the eastern and western hemispheres. Inspection of the longitude–height structure at different latitudes also reveals that the eastern hemisphere features are more barotropic than the western hemisphere features. At low levels, the wave pattern evidences a southwest–northeast tilt on the equatorward side of the jet, marking a net poleward wave momentum flux. Additionally, the high and low centers shift poleward by 10°–15° with increasing height, tracking the jet core's poleward shift.

The application of linear theory in the presence of Mars's large amplitude topography, particularly in the tropics, is perhaps an extreme that should be justified. To this end, we have determined a posteriori estimates of potential effects of nonlinearity (i.e., whether near-surface flow goes up and over versus around topographic barriers). Our estimates were obtained by computing, W, the "eddy interaction" term (cf. Holton 1975) defined by

$$W = (a\cos\varphi)^{-1}(u'_B h'_{B\lambda} - \overline{u'_B h'_{B\lambda}}) + a^{-1}(v'_B h'_{B\varphi} - \overline{v'_B h'_{B\varphi}}) \quad (14)$$

and comparing such estimates to the traditional *linear* kinematic boundary condition given by (10). Although determining the importance of nonlinearity in this way is not entirely consistent (i.e., estimating second-order effects from first-order deviations), it does provide a quantitative assessment as to where the assumptions of linearity may or may not be too restrictive. We find that the eddy interaction terms can be substantial in the eastern subtropics around Tharsis. The magnitudes $O(5$–10 cm s^{-1}) are as large as those from the linear boundary condition. However, in the winter extratropics (e.g., $\varphi > 20°$) vertical velocities from the linear boundary condition exceed the nonlinear estimates by an order of magnitude or more. This latitude band is the primary region of study in our linear analysis. A more consistent assessment would be one following Trenberth and Chen (1988), in which the wavenumbers of the forced response are coupled. Such an approach is beyond the scope of this work. We note that the zonal-mean topography is large on Mars, being $O(1$–3 km). It maximizes in low latitudes and slopes in both hemispheres toward middle and high latitudes. The occurrence of this slope may put linear modeling of stationary planetary in Mars's winter extratropics on a better footing. Results of Cook and Held (1992), who used a linear model in conjunction with a GCM in a controlled investigation of terrestrial stationary waves, have shown that linear theory begins to break down when topographic slopes exceed mean isentropic slopes. For Mars, the meridional topographic slope $h_{B\varphi}$ is very much dominated by the mean zonal slope $\bar{h}_{B0\varphi}$, and the latter is directed oppositely to the slope of isentropic surfaces, especially in the sub- and extratropics. Finally, comparisons of linearly predicted stationary wave amplitudes, phases, and horizontal wave patterns with those produced in the National Aeronautics and Space Administration (NASA)/Ames MGCM (Haberle et al. 1993; Barnes et al. 1993) show very comparable structures.

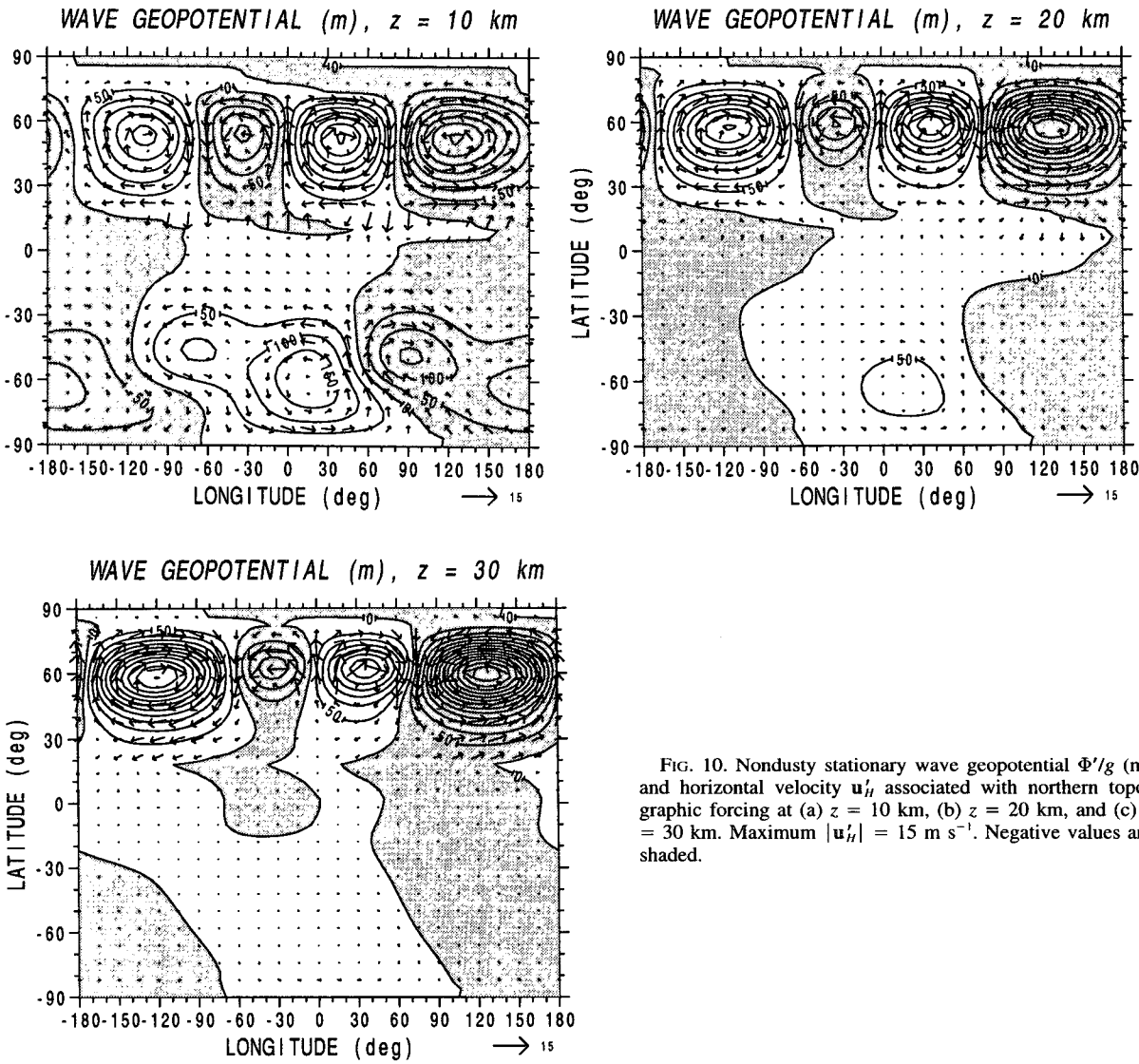

FIG. 10. Nondusty stationary wave geopotential Φ'/g (m) and horizontal velocity $\mathbf{u}'_H$ associated with northern topographic forcing at (a) z = 10 km, (b) z = 20 km, and (c) z = 30 km. Maximum $|\mathbf{u}'_H|$ = 15 m s^{-1}. Negative values are shaded.

b. Southern topographic response

MGCM simulations for southern winter indicate that the extratropical zonally symmetric circulation is almost a "mirror image" of the winter northern hemisphere circulation, although slightly less intense (Haberle et al. 1993). Thus, as a first approximation for southern winter conditions, the same nondusty basic state is applied. In addition, the same dissipation, forcing level, and other model parameters are used.

Shown in Fig. 11 are wave structures for wavenumbers 1 and 2. Associated with a much larger forcing amplitude in the southern extratropics, wavenumber 1 reaches a very sizeable amplitude. Wavenumber 2 is weaker and, as in the northern case, is strongly barotropic. Although the wavenumber 3 topography in midlatitudes is much larger in the southern hemisphere, this mode achieves a similar amplitude. Patterns of the EP flux for the southern topography experiment (not shown) indicate a stronger upward and equatorward flux from midlatitudes, resulting in a stronger flux convergence (D_F = −10 to −40 m s^{-1} day^{-1}) in high latitudes. Both quantities are more intense because of the structure of wavenumber 1: its amplitude is larger (and increases more rapidly with height), and its phase tilts farther westward. Under quasigeostrophic scaling these two effects, when combined, yield stronger F and D_F (e.g., Andrews et al. 1987).

A notable difference from the northern topographic wave pattern is the dominance of zonal wavenumber 1, even at low levels. This is clearly apparent in longitude–latitude sections indicated in Fig. 12. The pattern arises both from a basic state conducive to wave-

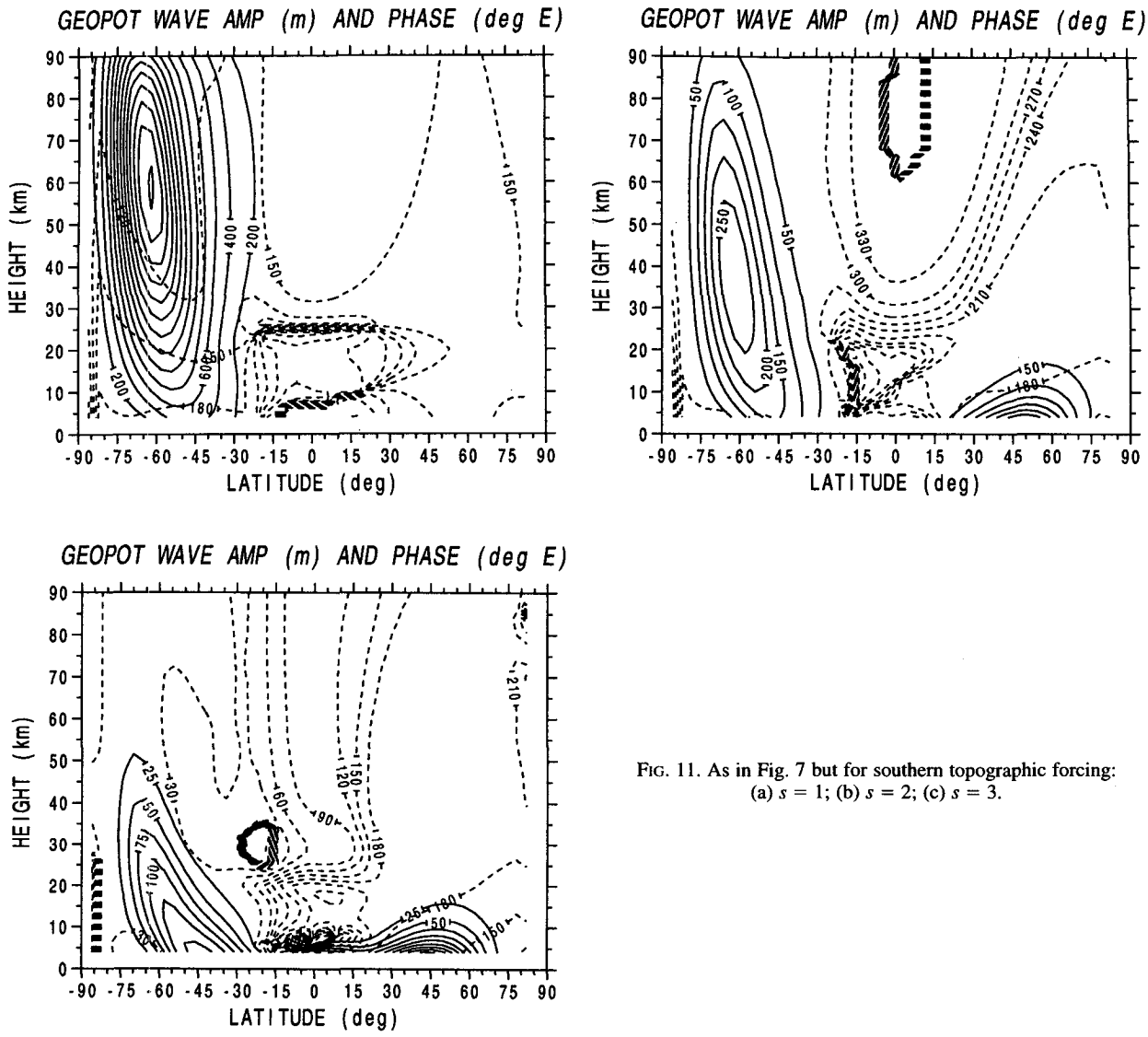

FIG. 11. As in Fig. 7 but for southern topographic forcing: (a) $s = 1$; (b) $s = 2$; (c) $s = 3$.

number 1 propagation and from a fortuitous distribution of wave forcing (there is almost 180° of longitude between Tharsis in the western hemisphere and Hellas in the eastern hemisphere). A trough is positioned asymmetrically about 0°E, which is flanked by a ridge to the east, centered near 150°E. At low levels (e.g., below 10 km) near 60°E, an intense cyclonic circulation can be seen in the vicinity of Hellas. With increasing height, the trough tilts southeast–northwest and substantially toward the west, supporting a poleward flux of momentum and heat. Peak to peak amplitude variations approach 2000 m at the 20-km level. In middle and high latitudes and extending up to high levels (e.g., 50–60 km), the southern stationary wave pattern evidences a more baroclinic response than in the northern hemisphere.

In both hemispheres, the positions of the stationary centers with respect to the underlying topography are generally consistent with theory of forced stationary planetary waves (e.g., Dickinson 1978, 1980; Grose and Hoskins 1979; Hoskins and Karoly 1981; Held 1983). For example, regions of high geopotential in northern midlatitudes are anchored to the high relief of Tharsis and Arabia Terra. A close inspection of the wave geopotential phases, however, indicates that in the northern extratropics and near the forcing level wavenumber 1 is shifted 20°–30° to the west of the wavenumber 1 topography while wavenumber 2 is very much in phase with the wavenumber 2 topography. For the southern experiment, the wavenumber 1 response is shifted farther west of the topography (by 30°–50° in midlatitudes), and the wavenumber 2 response is shifted only slightly to the west (between 5°–10°).

From a thermodynamic standpoint, the wave geopotential and vertical velocity suggest a near balance

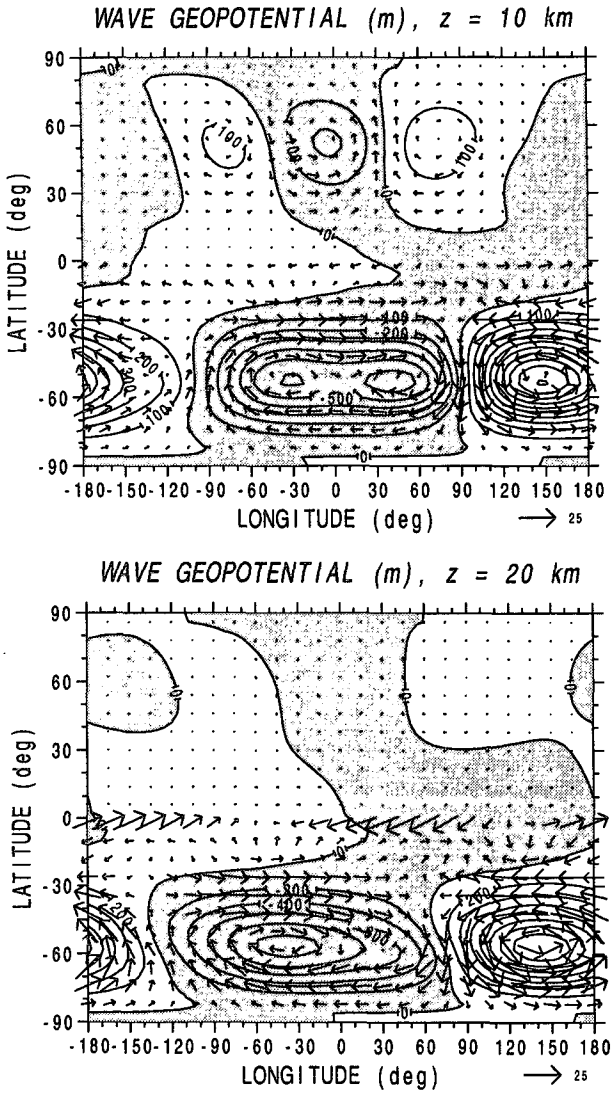

FIG. 12. As in Fig. 10 but for southern topographic forcing: (a) z = 10 km and (b) z = 20 km. Maximum $|\mathbf{u}'_H|$ = 25 m s^{-1}.

between horizontal advection and adiabatic cooling; that is, $v' \approx -(a\bar{\theta}_z/\bar{\theta}_\varphi)w'$, so that in the northern (southern) hemisphere we have $v' \sim +(-)\,\mathrm{sgn}(w')$. In the north, upward (downward) motion on the upstream (lee) side of Tharsis, Arabia Terra, and Elysium is accompanied by positive (negative) meridional wind. The strongest positive w' is located on the upstream side of Arabia Terra near 45°N, and the corresponding anticyclone, shifted slightly to the west of this relief, provides for warm advection to counteract adiabatic cooling of the ascending air. In the southern experiment, the strongest vertical motions occur to the west and east of Hellas. On the downslope between Noachis Terra and Hellas (near 40°E and −50°N), adiabatic warming is offset by equatorward flow from the cyclone centered just west of Hellas. As discussed by Hoskins and Karoly (1981), for a baroclinic atmosphere, horizontal advection by the zonal-mean zonal wind can displace the centers of high geopotential slightly toward the west (of the order 10°–20°, typically).

c. *Meridional confinement of wave trains*

In the above nominal topographic experiments, it is apparent that wave activity becomes "channeled" within a midlatitude band. Here, we use a more basic model of planetary wave meridional dispersion to illuminate the nature of this channeling.

Following Hoskins and Karoly (1981), using the linearized nondivergent barotropic vorticity equation in a Mercator projection of the sphere with allowance for $\bar{u} = \bar{u}(\varphi)$ and, assuming plane wave solutions, one can derive the dispersion relation

$$\omega = \tilde{u}k - \frac{\tilde{\beta}k}{k^2 + l^2}. \tag{15}$$

In the above, $\tilde{u} = \bar{u}/\cos\varphi$, and $\tilde{\beta} = \cos\varphi\{\beta - a^{-1}[(a\cos\varphi)^{-1}(\bar{u}\cos\varphi)_\varphi]_\varphi\}$. In the stationary case, k and l are constrained; namely, $l^2 = l^2(\varphi) = \tilde{\beta}/\tilde{u} - k^2$. As $l \to 0$, there is a "turning latitude" at which ray paths cease their poleward excursion. In this case, $k^2 = k_T^2 \equiv \tilde{\beta}/\tilde{u}$. Equivalently, the turning latitude can be expressed in terms of a nondimensional wavenumber as

$$s_T = ak_T = \cos\varphi\langle a\bar{u}^{-1}\{2\Omega\cos\varphi - [(a\cos\varphi)^{-1}(\bar{u}\cos\varphi)_\varphi]_\varphi\}\rangle^{1/2}. \tag{16}$$

Wave propagation (trapping) occurs in regions where $s < (>)\, s_T$ (Hoskins and Karoly 1981). Calculations of s_T for nondusty winter conditions on Mars may be done using the nominal nondusty basic state.

As can be seen in Fig. 13, s_T shows marked meridional variation even within the first few scale heights. This variation is due to a rapid increase in the curvature and intensity of the tilted jet with both latitude and height. Below 10 km, wave activity from planetary scales is free to propagate within a broad latitudinal band (φ = 20°–65°N). But by 20 km or so, a definite "cavity" exists in which wavenumber 2 can be confined between 35°–60°N. This forced wave "well" becomes very pronounced above 25 km: wave activity excited from wavenumbers 1–3 in midlatitudes cannot escape toward the tropics, nor can low-latitude, low-wavenumber activity penetrate into the extratropics. In the terrestrial northern winter atmosphere, typical climatological upper-tropospheric flows do not evidence such meridional confinement (Grose and Hoskins 1979; Held 1983). However, occasionally during southern winter, a midlatitude minimum in s_T can occur because of "double jet" structures (James 1988), which prevents all but the longest planetary scales excited in low latitudes from penetrating into high lati-

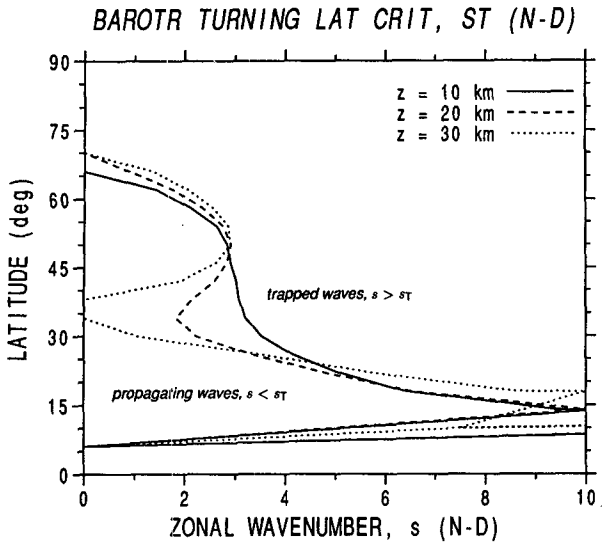

FIG. 13. Latitudinal variation of the barotropic turning latitude s_T as a function of zonal wavenumber (nondimensional).

tudes. In this regard, the winter atmosphere on Mars in both hemispheres may be an extreme example of the terrestrial southern winter condition.

5. Potential global responses and wave interference

In the previous section, it was found that topographically forced wavenumber 1 and 2 structures for Mars were not only quite vertically extended but also that the resulting horizontal wave patterns in the winter extratropics were channeled into a narrow latitude band. It is worthwhile to further investigate the "global" (i.e., appearing in both western and eastern hemispheres) and asymmetric nature of the forced response within simplified dynamical contexts and with idealized isolated forcings. By revealing the nature of the wave propagation in two and three dimensions, such an approach can aid in the interpretation of results from a more complete model.

a. One-dimensional barotropic predictions

Whether forced planetary waves on Mars might have large global responses can be investigated using a very basic 1D model. Under quasigeostrophic conditions and for a midlatitude β plane, the amplitude of a topographically forced height perturbation in a dissipative (vorticity damped) barotropic atmosphere is given by (e.g., Held 1983)

$$\hat{\eta} = \frac{\alpha \hat{h}_B}{\lambda^2[K^2 - K_s^2 - i\epsilon_r]}. \qquad (17)$$

In the steady, linearized potential vorticity equation, it is assumed that $\bar{u}$ = const, and a plane wave solution is sought: $\eta' = \mathrm{Re}\{\hat{\eta} e^{i(kx+ly-\omega t)}\}$. In (17), $\hat{\eta}$ is the amplitude of the free-surface height about the fluid's mean depth h_0; $\hat{h}_B$ is the amplitude of the surface topography; $K^2 = k^2 + l^2$ is the horizontal wavenumber; $K_s^2 \equiv \beta_T/\bar{u}$ is the resonant wavenumber; $\lambda^2 = gh_0/f_0^2$; $\epsilon_r = rK^2/k\bar{u}$; $\beta_T = \beta_0 - \bar{u}_{yy} + f_0\bar{h}_{By}/h_0$ is the mean vorticity gradient (assuming, as is the case for Mars, that mean meridional flow curvature and topographic slope are significant); r is a constant vorticity damping rate; and α is a positive constant less than one, chosen such that the low-level mean flow that interacts with the surface topography is a fraction of the upper-level flow.

The sensitivity of this 1D solution to choices of the mean flow, dissipation strength, meridional scale, latitude of the topography, etc. can be examined. As an example, the height variance using the smoothed Mars topography at 40°N is shown in Fig. 14 as a function of constant mean zonal wind and dissipation strength. In the calculation, h_0 = 10 km; al = 4.5; α = 0.3; and a plausible estimate of the effective beta is used, $\beta_T \approx (1 + M)\beta_0$. Based on a northern winter, nondusty mean zonal flow for Mars (e.g., as in Fig. 4a) and measurements of mean topographic slopes in midlatitudes, $M \approx 2$–4. For weak damping (e.g., time constants $r^{-1} > 3$ days), resonant responses are apparent and correspond to (for decreasing mean wind speed) zonal wavenumbers 1, 2, . . . , 5, respectively. For time constants smaller than 1–2 days, a broad response is produced between $\bar{u}$ = 40–60 m s^{-1}. This feature is associated with zonal wavenumbers 2 and 3. With weak dissipation and decreasing meridional scale, the other resonant features are "clustered" more closely around the wavenumber 2 and 3 response (i.e., the range of $\bar{u}$ is less), and its center is shifted toward weaker $\bar{u}$.

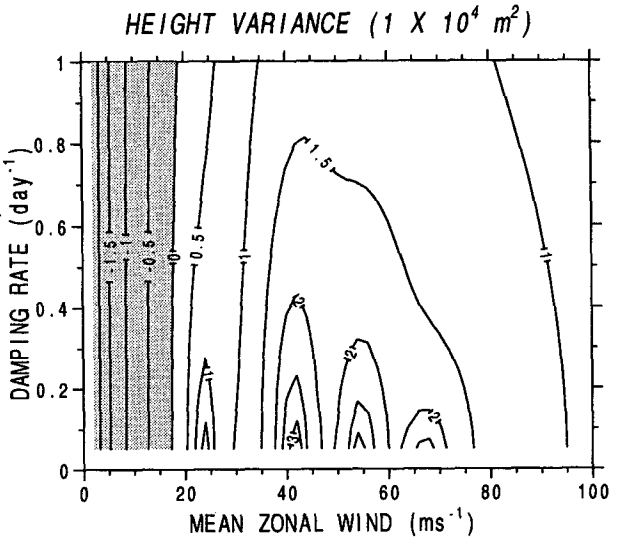

FIG. 14. Logarithm of the height variance $\overline{\eta'^2}$ (10^4 m^2) of the 1D barotropic solution as a function of dissipation and constant $\bar{u}$. Values less than 10^4 m^2 are shaded.

From this basic 1D barotropic model, *very* large stationary amplitudes are predicted for winterlike $\bar{u}$ on Mars, with peak to peak values of $O(1-3$ km) even in the presence of considerable dissipation (e.g., $r^{-1} = 1-5$ days).

b. Isolated topographies

For the 1D barotropic problem, the stationary solution as a function of longitude can be readily calculated, and this is shown for 40°N in Fig. 15. Here, $\bar{u} = 50$ m s^{-1}, $r^{-1} = 2$ days, and $al = 4.5$. It can be seen that the peak to peak response in the eastern hemisphere exceeds that in the western hemisphere by a factor of 2–3. This asymmetry is preserved even for very strong dissipation (e.g., $r^{-1} = 0.3$ day). The dashed and dotted curves show the solution when only the western or eastern hemisphere topography is included. Both global responses and wave train interference are evident. At this latitude, the strongest cancellation occurs near Tharsis, between −90° and −40°E. The choice $r^{-1} = 2$ days is an approximate threshold value as to whether substantial interference takes place. For $r^{-1} > 2$ days, the forced wave "ringing" produces secondary/tertiary responses downstream of the topography large enough that constructive/destructive reinforcement occurs. Expressed in another way, as the amount of dissipation is decreased, the position of the barotropic ridge is shifted farther westward of the major topographic upslope, for wavelengths both longer and shorter than the resonant wavelength $L_s^2 \equiv 4\pi^2\bar{u}/\beta_T$ (Hoskins and Karoly 1981).

One can estimate whether the forced response should be global in contrast to local by considering the ratio of the dissipation timescale to the energy propagation timescale; namely,

$$D = \frac{dc_g^{(x)}}{2\pi a \cos\varphi}, \tag{18}$$

where d is the dissipation timescale and $c_g^{(x)}$ is the zonal component of the group velocity. For $D \geq O(1)$, a global response may be expected; for $D \ll O(1)$, the response should be local. For stationary waves in the 1D barotropic case, $c_g^{(x)} = 2\bar{u}k^2/(k^2 + l^2)$, and with near-meridional trapping conditions in midlatitudes (i.e., where $l \to 0$ in the vicinity of the turning latitude), $c_g^{(x)} \sim 2\bar{u}$. For typical midlatitude values for Mars ($\varphi_0 = 50$°N, $\bar{u} \sim 100$ m s^{-1}, and $d \sim 3$ days), $D \sim 4$. In contrast, for the case of Earth ($\bar{u} \sim 15$ m s^{-1} and $d \sim 6$ days), $D \sim 0.6$. Under the assumptions of such a scaling argument, global responses ought to occur more readily in the Mars case. Very short dissipation timescales would be necessary for Mars's atmosphere to yield a D value much less than one.

1) SYNTHETIC THARSIS CASE

It is also useful to examine the contribution from Mars's dominant orographic feature, the Tharsis ridge.

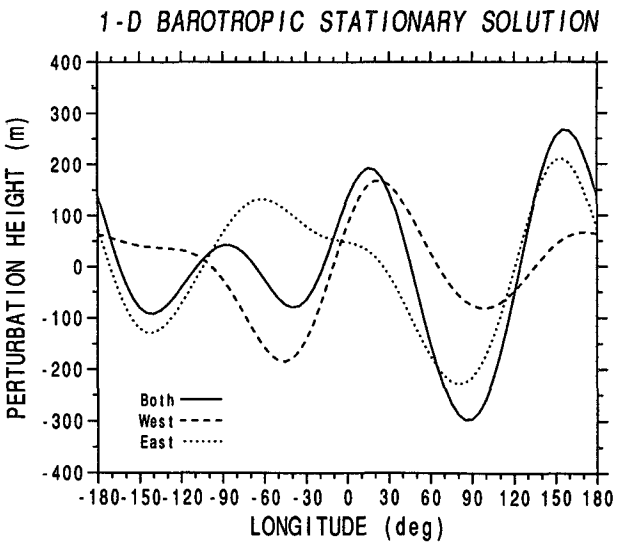

FIG. 15. Longitudinal variation at 40°N of the 1D barotropic solution for the disturbance height η' (m).

This may be done using a synthetic mountain in the spherical LPE model. The model mountain is a near-equatorial Gaussian ellipse constructed to represent Tharsis's bulk configuration at the largest zonal scales. It is centered at $\lambda = -105$°E and $\varphi = -10$°N, and its elliptical base is rotated 15° with respect to parallels of latitude. Figure 16a shows its horizontal extent. The semimajor and minor axes are 34° of latitude and 30° of longitude, respectively, and the maximum height is 10 km. When compared to the consortium topography (cf. Fig. 5), it can be seen that the idealized topography contains the western hemisphere's high relief reasonably well.

Shown in Fig. 16b is a longitude–latitude section of the wave geopotential forced from the isolated Tharsis. The same dissipation and forcing level of the consortium topography experiment were used. It can be seen that the horizontal pattern is dominantly zonal wavenumber 1, and it is again channeled within a finite latitude band. What is clearly demonstrated with the synthetic mountain is a large response far downstream of the source (e.g., between 120°–150°E), in general agreement with the 1D barotropic predictions. This downstream response can be reduced when stronger dissipation is used in the model [e.g., with α_R set to profile (i) in Fig. 2]. Compared to the western hemisphere high and low geopotential centers shown in Fig. 10, the ridge and trough from the isolated topography are broader zonally and shifted in phase. The phase difference arises from the trough formed in the lee of Elysium in the consortium experiment, which reduces the zonal scale of the ridge over Tharsis and shifts its center toward the east. Also, in the isolated Tharsis case the trough remains well above 50 km, whereas in the

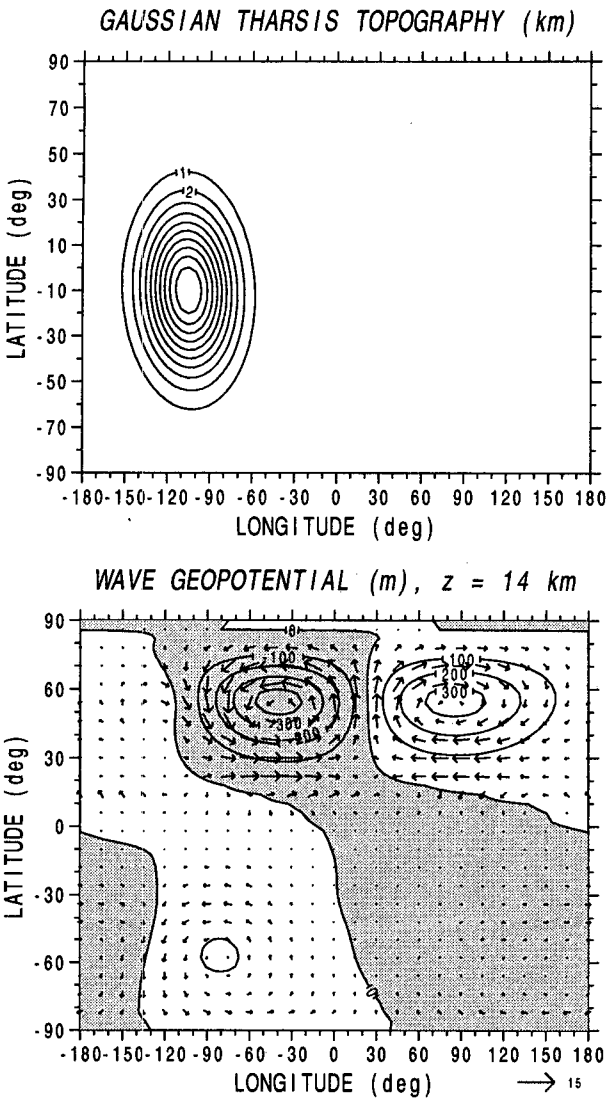

FIG. 16. As in Fig. 10 but for the isolated Tharsis experiment: (a) topography distribution (km) and (b) z = 14 km. Maximum $|\mathbf{u}'_H|$ = 15 m s^{-1}.

consortium experiment this feature mostly vanishes above 35 km.

2) EASTERN HEMISPHERE CASE

Motivated by results from section 4 indicating a hemispheric asymmetry in the topographic response and a mostly zonally oriented wave pattern, the topographic response to just the eastern topography is examined next. Figure 17 shows the horizontal wave pattern from such an experiment. At low levels, the pattern indicates a series of troughs and ridges emanating from near −30°E, 30°N that have a more poleward and eastward orientation compared to the isolated Tharsis or full-topography experiments. By 20 km, the topographic ridge over Arabia Terra is mostly replaced by a trough, and, in higher latitudes, the response downstream of the source is very large (note the large ridge at −140°E). The forced wave's more baroclinic structure, particularly in midlatitudes, is more clearly depicted in Fig. 18, which shows a longitude–height cross section of wave geopotential at 46°N. At low levels, the response peaks near the source, while farther downstream, the maximum occurs at upper levels (e.g., between 50 and 60 km).

The actual flux of wave activity in both horizontal and vertical directions can be viewed using a diagnostic of Plumb (1985). The Plumb flux, $\mathbf{P} = [P^{(\lambda)}, P^{(\varphi)}, P^{(z)}]$, is a 3D extension of the EP flux (valid under

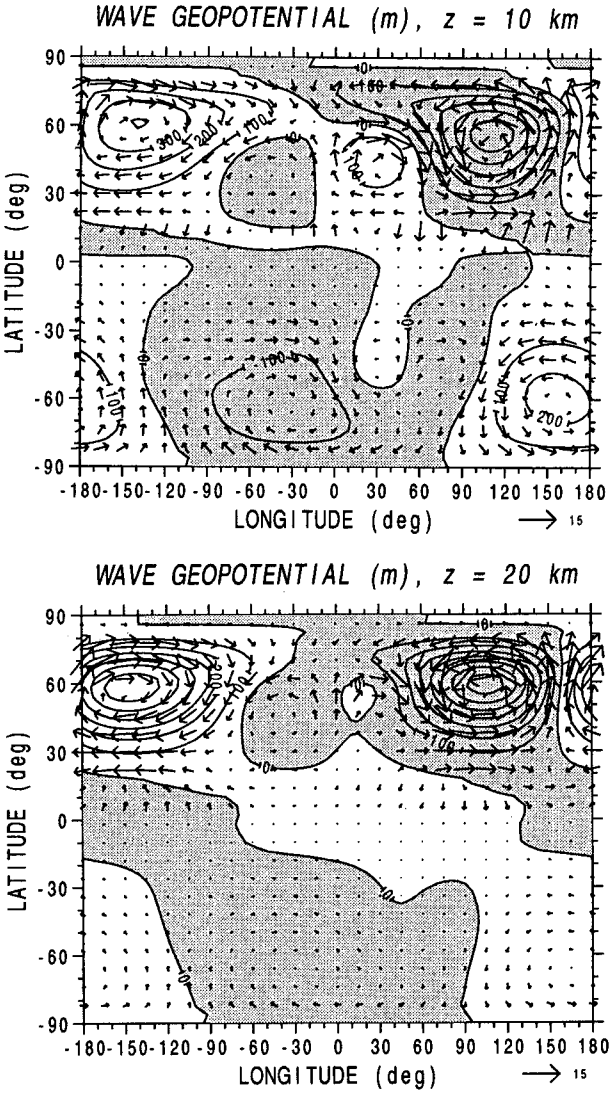

FIG. 17. As in Fig. 10 but for the eastern topography experiment: (a) z = 10 km and (b) z = 20 km. Maximum $|\mathbf{u}'_H|$ = 15 m s^{-1}.

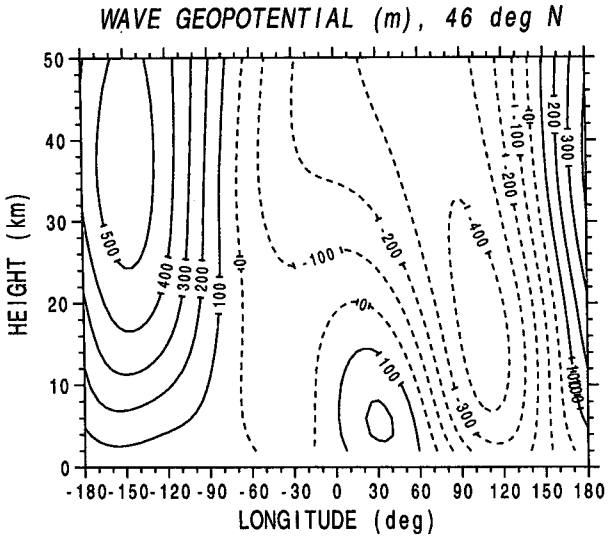

FIG. 18. Longitude–height structure at 46°N of the stationary geopotential Φ'/g (m) in the eastern topography experiment. Negative values are dashed.

quasigeostrophic assumptions) and has been successfully applied in both modeling (e.g., Marks 1988) and observational (e.g., Plumb 1985; Karoly et al. 1989) studies of terrestrial quasistationary planetary waves. Evidence for poleward and equatorward wave propagation can be seen in Fig. 19a, which is a plot of **P** as defined by (7.1) in Plumb (1985). Just downstream of the source, the vertical component $P^{(z)}$ is dominantly upward, away from the topography, and a split in the horizontal flux appears in the eastern hemisphere between 40°–50°N. Wave activity is drawn into high latitudes. Examination of **P** in the longitude–height plane (not shown) reveals that in midlatitudes the flux is generally upward and zonal within the waveguide. For comparison, the full topography experiment is shown in Fig. 19b. Wave trains excited in both eastern and western hemispheres interfere strongly in the horizontal and vertical directions, which results in a "turning" of the wave activity flux into a dominant upward and zonal direction in midlatitudes.

In summary, these experiments suggest that the equivalent barotropic wave structure seen in the full-topography experiment in midlatitudes must result from interference between wave trains excited in each hemisphere. The wave train interference in three dimensions is similar to that predicted from the 1D barotropic considerations, where significant wave amplitude cancellation occurred east of Tharsis. However, because of the tendency for meridional trapping within the mean basic state, the net flux of wave activity is channeled eastward—instead of poleward/equatorward—to produce enhanced zonal alignment of the stationary eddy fields.

6. Effects of dust

Strong differences in the intensity and meridional structure of the zonally symmetric flow during periods of enhanced atmospheric dustiness should affect the structures of Mars's northern winter stationary eddies. Using a synthetic "highly dusty" mean zonal flow, potential differences in the steady wave patterns can be investigated. As in the nondusty experiment, the forcing is imposed at z_B. Equal Newtonian cooling and Rayleigh friction are used [profile (i) in Fig. 2] that provide substantial dissipation below 25 km where damping rates are $O(1-5$ days).

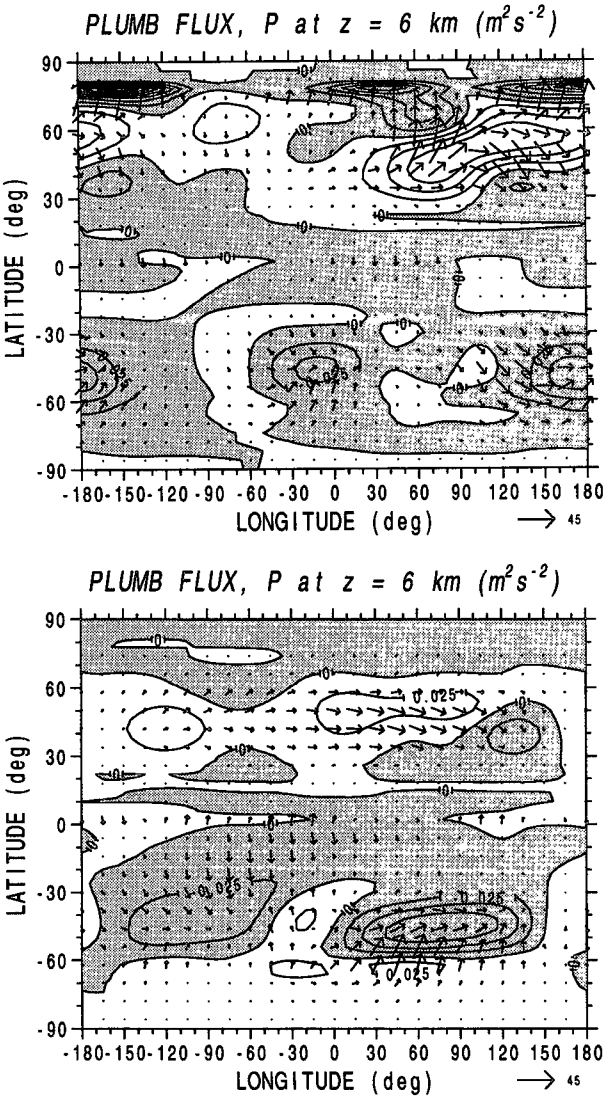

FIG. 19. Nondusty Plumb flux P (m^2 s^{-2}) associated with northern topography experiments. Vectors are the (λ, φ) components at 6 km, and contours are the (z) component, with negative (downward) shaded: (a) eastern topography only and (b) full topography.

a. Northern topographic forcing

Shown in Fig. 20 are the wave geopotential amplitudes for wavenumbers 1 and 2. Also shown are the corresponding refractive index patterns. In the dusty basic state, wavenumber 1 is stronger (by a factor of 3–4), is narrower meridionally, and peaks farther north and at higher levels than in the nondusty flow. Sensitivity experiments similar to those done for the nondusty basic state indicate that the location of the peak wavenumber 1 response is insensitive to the strength of the dissipation above 50–60 km. In contrast, wavenumber 2 evidences strong vertical trapping, with the amplitude becoming "squashed" in midlatitudes. For higher wavenumbers, little propagation occurs. What wave activity does propagate upward is confined to midlatitudes below 10–15 km.

The dusty amplitude structures are tied closely to the refractive indexes $\tilde{Q}_s$ associated with this basic state. Like the flow itself, the centers of the waveguides are shifted 5°–10° poleward, and compared to the nondusty patterns, the positive regions through the jet are narrower. For wavenumber 1, the enhanced waveguide through the jet core [associated with larger $\bar{q}_\varphi/\bar{u}$, i.e., very strong (negative) meridional curvature and more (positive) vertical shear], results in strong propagation of wave activity upward into high latitudes. This enhanced waveguide effect bears some analogy with the terrestrial atmosphere, in particular, the sensitivity of extratropical stationary wave propagation to latitudinal shifts in the subtropical jet (Nigam and Lindzen 1989). In earth's case, equatorward displacement of the subtropical jet and concomitant changes in the refractive index can facilitate meridional propagation of wave activity into high latitudes. In the Mars case, intensification of the zonally symmetric circulation during dusty conditions and slight poleward shift of the westerly jet enhances the extratropical refractive index, which can facilitate wave propagation aloft.

The poleward and upward flux (equatorward momentum and poleward heat flux) are regulated by the wave's latitudinal and vertical phase variation. Between 40°–65°N near the forcing level, the phase tilts westward with increasing latitude and, between 60°–80°N and above 10 km, the phase tilts westward with increasing height. Both the waveguide and phase variation permit wave activity to penetrate upward into high latitudes (Palmer 1982), so that, even in the presence of much stronger dissipation, wavenumber 1 achieves a far greater amplitude than in the nondusty experiment. However, higher wavenumbers having vertically restrictive waveguides are inhibited.

Accompanying the large wavenumber 1 amplitude is a strong high-latitude EP flux convergence. In polar latitudes the net wave activity flux results in a steady, mean zonal deceleration of $\bar{u}_t \sim -20$ m s^{-1} day^{-1} at upper levels. If the mean zonal flow could decelerate, the residual mean meridional circulation would act to maintain thermal (gradient wind) balance. For example, for a "decelerated" mean zonal flow, a poleward and downward circulation would ensue, producing thermal tendencies $\bar{T}_t = 2$–4 K day^{-1} in high latitudes between 30–50 km. The bulk of the warming would be due to descent (i.e., $\bar{w}^* < 0$) and compressional heating. Although this thermal tendency is for steady conditions, its magnitude is comparable to that observed by the *Viking* Infrared Thermal Mapper near the 25-km level over the polar region during a winter solstice global dust storm (Martin and Kieffer 1979; Jakosky and Martin 1987). Time-dependent, forced wave calculations in spherical geometry for highly dusty conditions (to be reported in a future paper) indicate that wave transience can produce even larger thermal tendencies in high latitudes and that the location of peak warming descends with time.

For the dusty basic state, the horizontal wave patterns are quite different than for the nondusty basic state. As shown in Fig. 21, high and low geopotential are again centered in the extratropics, with a dominant zonal wavenumber 2 pattern at low/middle levels. Above 20–25 km, however, the dominant zonal wave pattern rapidly becomes wavenumber 1. Tracking the dusty jet core, the centers themselves are shifted roughly 10° farther poleward. South of 45°N and below 20 km, the dusty stationary waves exhibit stronger southwest–northeast tilting than the nondusty stationary waves, indicative of larger poleward momentum flux. The longitude–height structure of the dusty stationary waves (not shown) reveals that, particularly in the subtropics and midlatitudes, the waves exhibit stronger westward phase tilt with height. And in high latitudes below 40 km, the total wave field in the eastern hemisphere evidences more westward tilt, compared to the barotropic structure in the nondusty case.

Comparison of the low-level wave phase with respect to the topographic forcing reveals further differences with the nondusty response. For example, in the subtropics and midlatitudes, wavenumber 2 is now slightly out of phase with less than a 10° westward shift. On the other hand, wavenumber 1 shows considerable phase shift with latitude. In the subtropics and high latitudes, wavenumber 1 is west of the forcing by 20°–60°. Within the zonal waveguide (between 50°–75°N), the phase shift is larger and approaches ~180° at 65°N. The occurrence of a very large wavenumber 1 amplitude in high polar altitudes, little vertical phase variation between 50° and 65°N above 15–20 km, and a nearly 180° phase shift of the response with respect to the forcing are indicators that wavenumber 1 could be at (or near) resonance in the dusty basic state. With simple choices for mean flows and dissipation (e.g., constant vertical shear and damping) in quasigeostrophic β-plane models, similar characteristics are found for modes with zonal scales larger than the resonant wavelength (e.g., Held 1983).

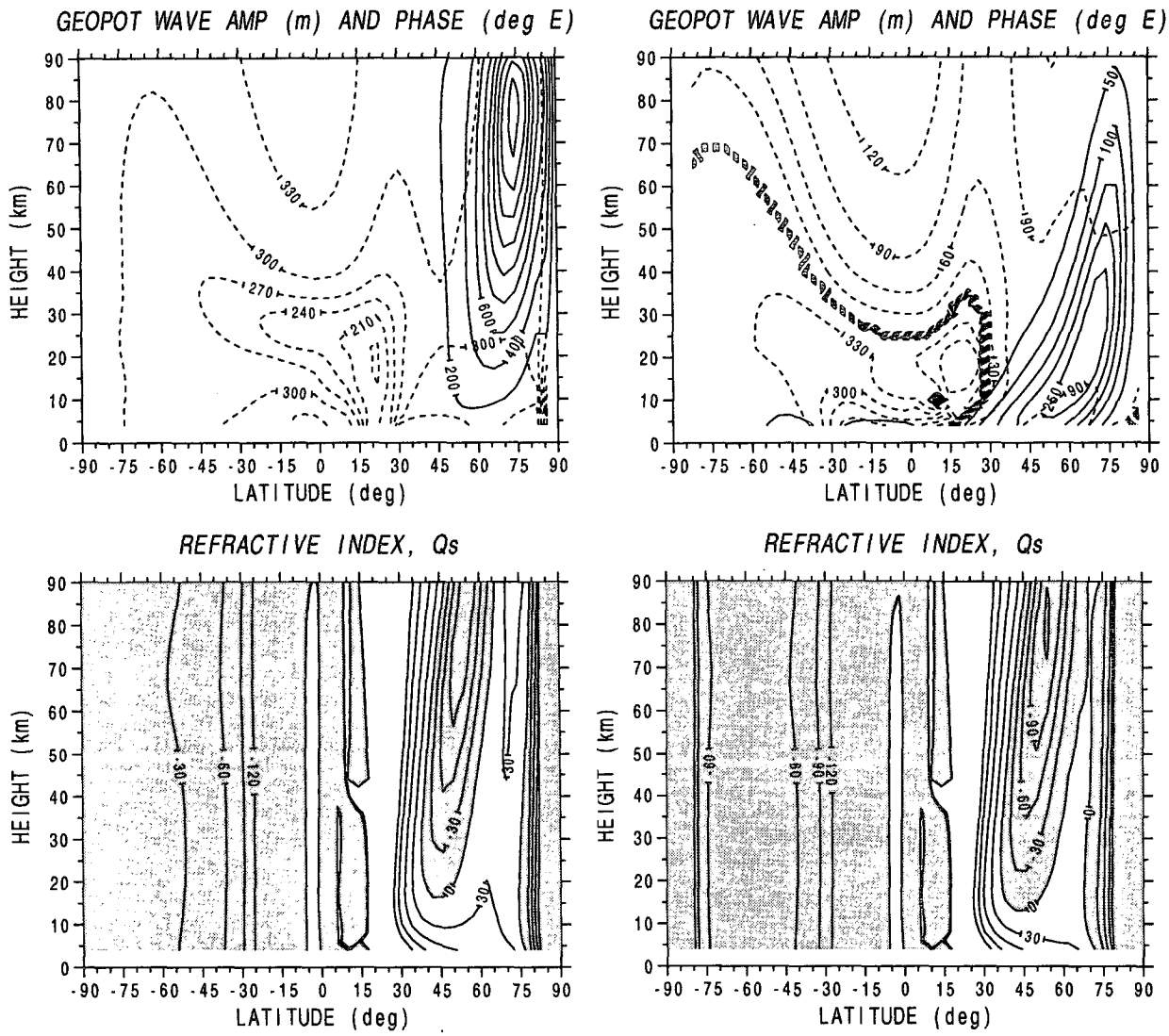

FIG. 20. As in Figs. 7 and 8 but for the dusty basic state: (a) $s = 1$; (b) $s = 2$; (c) $s = 1$; (d) $s = 2$.

Several sensitivity experiments were performed to investigate the robustness of a large wavenumber 1 response to changes in the dissipation and in the dusty basic state. For weaker dissipation [α_R set to profile (h) or (j) in Fig. 2] amplitudes ranged from 4000 to 8000 m in high polar altitudes. The effects of partial reflection/absorption from tropical easterlies (Nigam and Held 1983) was examined using a dusty basic state without the low-latitude critical surface but with the poleward-shifted waveguide. More low-level, low-latitude wave activity flux occurred in this case, yet the high-latitude structure was very similar: the maximum amplitude approached 5000 m, and the response was almost completely out of phase with the topography. A stronger dusty basic state was also used, one where the jet core approached 170 m s^{-1}. Wavenumber 1 reached a slightly weaker peak amplitude at high levels and exhibited an eastward phase tilt above 50–60 km in high latitudes. Such characteristics are consistent with partially impeded wave propagation for a very strong mean flow.

b. Long period, near-resonant modes?

The above results indicating a large-amplitude wavenumber 1 response, and the nature of its structure suggests that under dusty conditions the Mars winter atmosphere may approach conditions of resonance. By resonance, it is meant that a possible large-scale "free" or "forced" mode may be efficiently excited and, in the presence of dissipation, manifest itself in a large finite-amplitude response. The possibility of sta-

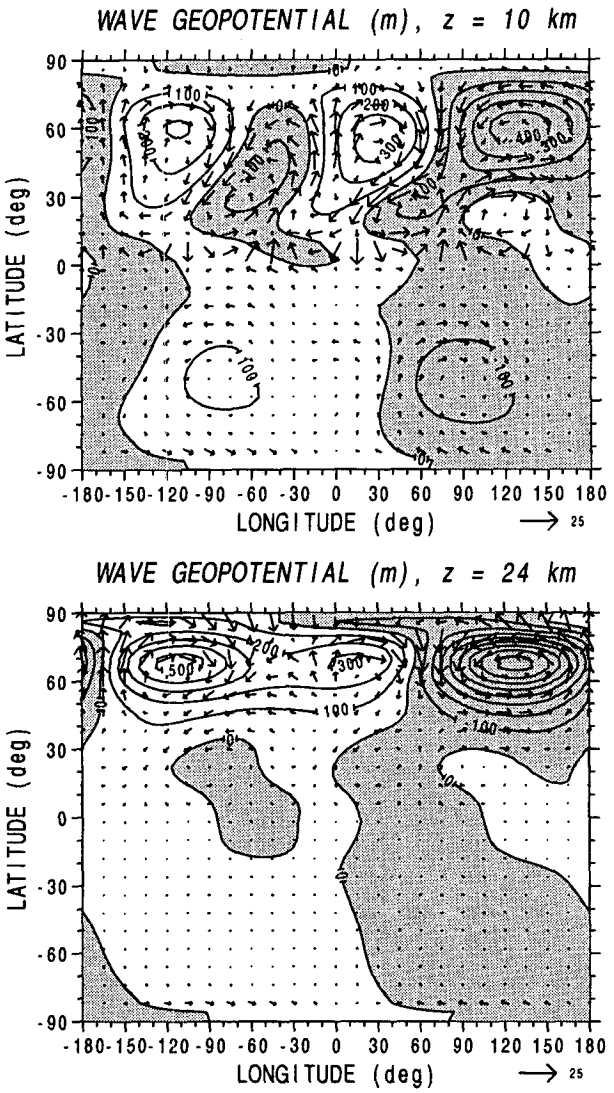

FIG. 21. As in Figs. 10 but for the dusty basic state: (a) z = 10 km and (b) z = 24 km. Maximum $|u_H'|$ = 25 m s^{-1}.

tionary (or low frequency) wavenumber 1 resonances [i.e., "characteristic" modes, as denoted by Salby (1981a,b)] can be investigated with the spherical LPE model. The procedure we apply is as follows.

In order to excite any modes associated with a particular mean basic state, a simple "forcing" is imposed at the model's lower boundary $z = z_B$. A nonzero vertical velocity $w' = \mathrm{Re}\{\hat{W}_s^{\sigma}(\phi, z)e^{i(s\lambda - 2\Omega\sigma t)}\}$ is specified with a constant amplitude, $\hat{W}_s^{\sigma} = 1$ cm s^{-1} (i.e., no latitude dependence is inserted into the problem at the lower boundary). While stepping through frequencies discretely, the magnitude of the wave response is monitored for quasi resonances using as a wave measure maximum $|\Phi'|$, $z \leq 60$ km. This examines the maximum wave geopotential amplitude associated with a given wavenumber and frequency within the region of interest. Calculations are made over a frequency range of $|\nu| \leq 0.2$ day^{-1}, with steps in frequency of $\Delta\nu = 0.005$ day^{-1}. Dissipation is applied using equal and constant rate coefficients for Newtonian cooling and Rayleigh friction.

In Fig. 22 response curves for the nondusty and dusty basic states are shown for wavenumber 1. A dissipation timescale of $\alpha_N^{-1} = 5$ days was imposed. For a range of low frequencies (e.g., periods longer than 20 days), the dusty response exceeds the nondusty response by an order of magnitude or more. Although the response near the stationary frequency is rather "broad" for both basic states, the accentuated response of the dusty basic state remains for a range of dissipation choices (e.g., $\alpha_N^{-1} \geq 1$ day). And with much stronger dissipation, the response near the stationary frequency does flatten yet still exceeds the nondusty case by a factor of 5.

For an intensified, mean circulation associated with dusty episodes during northern winter, we find that forced stationary wave activity can become highly amplified in the winter extratropics. In particular, very significant enhancement of wavenumber 1 can occur. Whether wavenumber 2 is also enhanced ultimately depends on the degree of meridional trapping in the winter extratropics. The actual magnitude of the stationary wave amplitudes will most certainly be a function of the strength and structure of the dusty waveguide (i.e., $\bar{q}_\varphi/\bar{u}$) and the effective dissipation present. In contrast, the magnitudes may only be weakly dependent on the wave sources in the extratropics.

7. Summary and conclusions

To recapitulate the main results of this study, Mars's winter extratropics should be characterized by large-

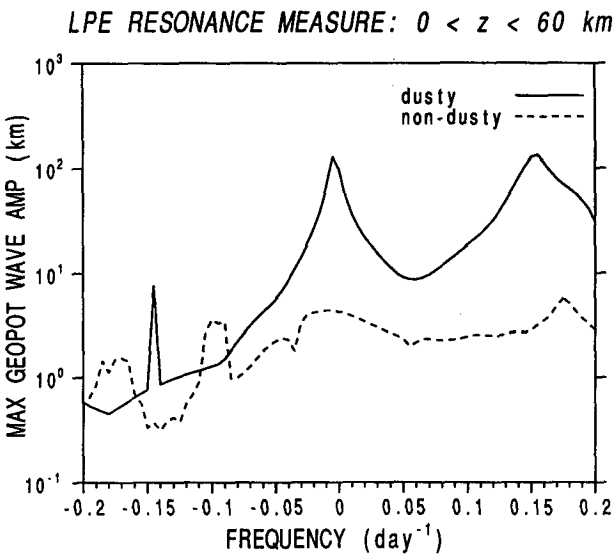

FIG. 22. Maximum wavenumber 1 response (km) as a function of frequency for the dusty (solid) and the nondusty (dashed) basic states for α_N^{-1} = 5 days.

amplitude, stationary Rossby modes. For wavenumbers 1 and 2 these waves show very deep vertical structure. In addition, there are substantial asymmetries between northern and southern stationary eddies (the latter are larger by a factor of 1–3). There are also east–west asymmetries in the basic response in northern midlatitudes, with the eastern region associated with stronger stationary low and high geopotential centers.

Strong interferences occur for wintertime stationary waves on Mars, even in the presence of large dissipation compared to Earth. The interferences are associated with large values of the zonal group velocity and a relatively small planet. They can occur both because of "modal beats" and from beats arising from different driving forces. Fundamental to the existence of global responses and wave interferences in the extratropics is a planetary waveguide formed by the mean zonal flow that causes significant meridional confinement within 2–3 scale heights of the surface.

For global-scale dusty episodes that are associated with an intensification of the zonal-mean circulation and a poleward shift of the jet, the LPE calculations indicate that a substantial enhancement of wavenumber 1 occurs. For nominal choices of parameters representative of such dusty conditions, quasi-stationary wavenumber 1 may in fact be near resonance (in the presence of strong dissipation).

Several aspects of the linear stationary wave results have been compared with winter solstice simulations from an improved version of the NASA/Ames MGCM that have used the Mars Consortium topography. Qualitatively, the linear wave patterns are similar to patterns found in the MGCM: a predominant wavenumber 2 pattern in the northern winter extratropics, a large wavenumber 1 pattern in the southern winter hemisphere, and for highly dusty simulations, a large amplification of wavenumber 1. There are also asymmetries between the eastern and western hemispheres in the northern winter nondusty MGCM simulations. Quantitatively, detailed comparisons are somewhat dubious since the vertical coordinates and physical parameterizations are not the same and the MGCM zonal-mean zonal wind fields differ from those used in the LPE model. Such differences between the two models most likely account for quantitative differences in the predicted wave amplitudes, phase shifts between the dominant extratropical ridge/trough centers, and subtropical discrepancies.

Undoubtedly, the character of Mars's winter stationary waves has important implications for the planet's present-day climate cycles regarding carbon dioxide, water vapor, and atmospheric dust. As demonstrated in the previous sections, large global responses and effects of wave interference effectively connect the eastern and western hemispheres of the winter atmosphere. In addition, a predominant zonally oriented steady wave pattern will most certainly influence the existence of an east–west winter "storm track" for Mars and the development and decay of transient baroclinic eddies. Further, asymmetries between the northern and southern winter stationary waves fundamentally implies asymmetries in the winter transient eddies of both hemispheres. And such asymmetries necessarily imply asymmetries in poleward transports of momentum and heat (e.g., Pollack et al. 1990) as well as atmospheric dust and suspended water vapor/condensate (e.g., Jakosky and Haberle 1992). The present-day climate cycles are all sensitive to any external asymmetries, and thus Mars's sub- and extratropical stationary eddies can be expected to play a key role over intraseasonal and interannual timescales.

Acknowledgments. This paper forms part of a doctoral dissertation completed by the first author at Oregon State University (OSU). The authors wish to acknowledge helpful comments by R. M. Haberle and R. E. Young that led to an improved manuscript and D. Vickers at OSU for performing the topography harmonic analysis and generous consulting regarding graphics. This research has been supported by the NASA Graduate Student Researchers Program under Grant NGT-50167. Additional funding was made available by the NASA Planetary Atmospheres Program (provided by Grants NAGW-727 and NAGW-1127) and the National Research Council.

REFERENCES

Albee, A. L., and D. F. Palluconi, 1990: Mars Observer's Global Mapping Mission. *Trans. Amer. Geophys. Union,* **71,** 1099; 1107.

Andrews, D. G., J. R. Holton, and C. B. Leovy, 1987: *Middle Atmosphere Dynamics.* Academic Press, 489 pp.

Barnes, J. R., 1984: Linear baroclinic instability in the Martian atmosphere. *J. Atmos. Sci.,* **41,** 1536–1550.

——, J. B. Pollack, R. M. Haberle, R. W. Zurek, C. B. Leovy, H. Lee, and J. Schaeffer, 1993: Mars atmospheric dynamics as simulated by the NASA–Ames general circulation model II. Transient baroclinic eddies. *J. Geophys. Res.,* **98,** 3125–3148.

Blumsack, S. L., 1971: On the effects of topography on planetary atmospheric circulation. *J. Atmos. Sci.,* **28,** 1134–1143.

Butchart, N., S. A. Clough, T. N. Palmer, and P. J. Trevelyan, 1982: Simulations of an observed stratospheric warming with quasi-geostrophic refractive index as a model diagnostic. *Quart. J. Roy. Meteor. Soc.,* **108,** 475–502.

Charney, J. G., and P. G. Drazin, 1961: Propagation of planetary-scale disturbances from the lower into the upper atmosphere. *J. Geophys. Res.,* **66,** 83–109.

Conrath, B. J., 1981: Planetary-scale wave structure in the Martian atmosphere. *Icarus,* **48,** 246–255.

——, and Coauthors, 1973: Atmospheric and surface properties of Mars obtained by infrared spectroscopy on *Mariner 9. J. Geophys. Res.,* **78,** 4267–4278.

Cook, K. H., and I. M. Held, 1992: The stationary response to large-scale orography in a general circulation model and a linear model. *J. Atmos. Sci.,* **49,** 525–539.

Dickinson, R. E., 1978: Rossby Waves—Long-period oscillations of oceans and atmospheres. *Annu. Rev. Fluid Mech.,* **10,** 159–195.

——, 1980: Planetary waves: Theory and observation. Orographic effects in planetary flows, GARP Publ. Ser. 23, World Meteorological Organization, 51–84.

Dunkerton, T. J., C.-P. F. Hsu, and M. E. McIntyre, 1981: Some Eulerian and Lagrangian diagnostics for a model stratospheric warming. *J. Atmos. Sci.,* **38,** 819–843.

Edmon, H. J., B. J. Hoskins, and M. E. McIntyre, 1980: Eliassen–Palm cross sections for the troposphere. *J. Atmos. Sci.*, **37**, 2600–2616.

Gadian, A. M., 1978: The dynamics of and the heat transfer by baroclinic eddies and large-scale stationary topographically forced long waves in the Martian atmosphere. *Icarus*, **33**, 454–465.

Grose, W. L., and B. J. Hoskins, 1979: On the influence of orography on large-scale atmospheric flow. *J. Atmos. Sci.*, **36**, 223–234.

Haberle, R. M., C. B. Leovy, and J. B. Pollack, 1982: Some effects of global dust storms on the atmospheric circulation of Mars. *Icarus*, **50**, 322–367.

——, J. B. Pollack, J. R. Barnes, R. W. Zurek, C. B. Leovy, J. R. Murphy, H. Lee, and J. Schaeffer, 1993: Mars atmospheric dynamics as simulated by the NASA–Ames general circulation model I. The zonal-mean circulation. *J. Geophys. Res.*, **98**, 3093–3124.

Hanel, R., and Coauthors, 1972: Investigation of the Martian environment by infrared spectroscopy on *Mariner 9*. *Icarus*, **17**, 423–442.

Held, I. M., 1983: Stationary and quasi-stationary eddies in the extratropical troposphere: Theory. *Large-Scale Dynamical Processes in the Atmosphere*, B. Hoskins and R. Pearce, Eds., Academic Press, 127–168.

Hollingsworth, J. L., 1992: Modeling of forced planetary waves in the Mars atmosphere. Ph.D. dissertation, Oregon State University, 318 pp.

Holton, J. R., 1975: *The Dynamic Meteorology of the Stratosphere and Mesosphere*. Meteor. Monogr. No. 37, Amer. Meteor. Soc., 218 pp.

Hoskins, B. J., and D. J. Karoly, 1981: The steady linear response of a spherical atmosphere to thermal and orographic forcing. *J. Atmos. Sci.*, **38**, 1179–1196.

Jakosky, B. M., and T. Z. Martin, 1987: Mars: North-polar atmospheric warming during dust storms. *Icarus*, **72**, 528–534.

——, and R. M. Haberle, 1992: The seasonal behavior of water on Mars. *Mars*, H. H. Kieffer, B. M. Jakosky, C. W. Snyder, and M. S. Matthews, Eds., University of Arizona Press, 969–1016.

James, I. N., 1988: On the forcing of planetary-scale Rossby waves by Antarctica. *Quart. J. Roy. Meteor. Soc.*, **114**, 619–637.

Karoly, D. J., R. A. Plumb, and M.-F. Ting, 1989: Examples of the horizontal propagation of quasi-stationary waves. *J. Atmos. Sci.*, **46**, 2802–2811.

Kieffer, H. H., P. A. Davis, and L. A. Soderblom, 1982: Mars' global properties: Maps and applications. *Proc. Lunar Planet. Sci. Conf.*, **12**, Pergamon Press, 1395–1417.

Leovy, C. B., 1985: The general circulation of Mars: Models and observations. *Advances in Geophysics*, Vol. 28A, Academic Press, 327–346.

——, and Y. Mintz, 1969: Numerical simulation of the atmospheric circulation and climate of Mars. *J. Atmos. Sci.*, **26**, 1167–1190.

Lin, B.-D., 1982: The behavior of winter stationary planetary waves forced by topography and diabatic heating. *J. Atmos. Sci.*, **39**, 1206–1226; corrigendum, **40**, 2321.

Lindzen, R. S., and H. L. Kuo, 1969: A reliable method for the numerical integration of a large class of ordinary and partial differential equations. *Mon. Wea. Rev.*, **97**, 732–734.

Marks, C. J., 1988: Linear wavetrains in models of the stratosphere. *Quart. J. Roy. Meteor. Soc.*, **114**, 297–323.

Martin, T. Z., and H. H. Kieffer, 1979: Thermal infrared properties of the Martian atmosphere II: The 15-μm band measurements. *J. Geophys. Res.*, **84**, 2843–2852.

Mass, C., and C. Sagan, 1976: A numerical circulation model with topography for the Martian southern hemisphere. *J. Atmos. Sci.*, **33**, 1418–1430.

Michelangeli, D. V., R. W. Zurek, and L. S. Elson, 1987: Barotropic instability of midlatitude zonal jets on Mars, Earth and Venus. *J. Atmos. Sci.*, **44**, 2031–2041.

Moriyama, S., and T. Iwashima, 1980: A spectral model of the atmospheric general circulation of Mars: A numerical experiment including the effects of the suspended dust and the topography. *J. Geophys. Res.*, **85**, 2847–2860.

Nigam, S., and I. M. Held, 1983: The influence of a critical line on topographically forced stationary waves in a barotropic model. *J. Atmos. Sci.*, **40**, 2610–2622.

——, and R. S. Lindzen, 1989: The sensitivity of stationary waves to variations in the basic state zonal flow. *J. Atmos. Sci.*, **46**, 1746–1768.

Palmer, T. N., 1981: Aspects of stratospheric sudden warmings studied from a transformed Eulerian-mean viewpoint. *J. Geophys. Res.*, **86**, 9679–9687.

——, 1982: Properties of the Eliassen–Palm flux for planetary scale motions. *J. Atmos. Sci.*, **39**, 992–997.

Plumb, R. A., 1985: On the three-dimensional propagation of stationary waves. *J. Atmos. Sci.*, **42**, 217–229.

Pollack, J. B., C. B. Leovy, P. W. Greiman, and Y. Mintz, 1981: A Martian general circulation experiment with large topography. *J. Atmos. Sci.*, **38**, 3–29.

——, R. M. Haberle, J. Schaeffer, and H. Lee, 1990: Simulations of the general circulation of the Martian atmosphere I: Polar processes. *J. Geophys. Res.*, **95**, 1447–1474.

Salby, M. L., 1981a: Rossby normal modes in nonuniform background configurations. Part I: Simple fields. *J. Atmos. Sci.*, **38**, 1803–1826.

——, 1981b: Rossby normal modes in nonuniform background configurations. Part II: Equinox and solstice conditions. *J. Atmos. Sci.*, **38**, 1827–1840.

Santee, M., and D. Crisp, 1993: Thermal structure and dust loading of the Martian atmosphere during late southern summer: *Mariner 9* revisited. *J. Geophys. Res.*, **98**, 3261–3279.

Schoeberl, M. R., and M. A. Geller, 1977: A calculation of the structure of stationary planetary waves in winter. *J. Atmos. Sci.*, **34**, 1235–1255.

Trenberth, K. E., and S.-C. Chen, 1988: Planetary waves kinematically forced by Himalayan orography. *J. Atmos. Sci.*, **45**, 2934–2948.

Webster, P. J., 1977: The low-latitude circulation of Mars. *Icarus*, **30**, 626–649.

Wu, S. S. C., 1978: Mars synthetic topographic mapping. *Icarus*, **33**, 417–440.